



City Research Online

City, University of London Institutional Repository

Citation: Qian, K., Liang, S-L., Feng, D-C., Fu, F. ORCID: 0000-0002-9176-8159 and Wu, G. (2020). Experimental and Numerical Investigation on Progressive Collapse Resistance of Post-tensioned Precast Concrete Beam-Column Sub-assemblages. *Journal of Structural Engineering*,

This is the accepted version of the paper.

This version of the publication may differ from the final published version.

Permanent repository link: <https://openaccess.city.ac.uk/id/eprint/23797/>

Link to published version:

Copyright and reuse: City Research Online aims to make research outputs of City, University of London available to a wider audience. Copyright and Moral Rights remain with the author(s) and/or copyright holders. URLs from City Research Online may be freely distributed and linked to.

City Research Online:

<http://openaccess.city.ac.uk/>

publications@city.ac.uk

1 **Experimental and Numerical Investigation on Progressive Collapse Resistance of** 2 **Post-tensioned Precast Concrete Beam-Column Sub-assemblages**

3 Kai Qian¹ M. ASCE, Shi-Lin Liang², De-Cheng Feng³, Feng Fu⁴ M. ASCE, and Gang Wu⁵

4 **ABSTRACT**

5 In this paper, four 1/2 scaled precast concrete (PC) beam-column sub-assemblages with high
6 performance connection were tested under push-down loading procedure to study the load resisting
7 mechanism of PC frames subjected to different column removal scenarios. The parameters investigated
8 include the location of column removal and effective prestress in tendons. The test results indicated that
9 the failure modes of unbonded post-tensioned precast concrete (PTPC) frames were different from that of
10 reinforced concrete (RC) frames: no cracks formed in the beams and wide opening formed near the beam
11 to column interfaces. For specimens without overhanging beams, the failure of side column was eccentric
12 compression failure. Moreover, the load resisting mechanisms in PC frames were significantly different
13 from that of RC frames: the compressive arch action (CAA) developed in concrete during column
14 removal was mainly due to actively applied pre-compressive stress in the concrete; CAA will not vanish
15 when severe crush in concrete occurred. Thus, it may provide negative contribution for load resistance
16 when the displacement exceeds one-beam depth; the tensile force developed in the tendons could provide
17 catenary action from the beginning of the test. Moreover, to deeper understand the behavior of tested
18 specimens, numerical analyses were carried out. The effects of concrete strength, axial compression ratio
19 at side columns, and loading approaches on the behavior of the sub-assemblages were also investigated
20 based on validated numerical analysis.

21 **Author Keywords:** Progressive Collapse; Precast Concrete; Load Resisting Mechanism;
22 Beam-Column Sub-assemblage

23
24 ¹Professor, College of Civil Engineering and Architecture at Guangxi University, Nanning, China 530004

25 (corresponding author), qiankai@gxu.edu.cn

26 ²Research Student, College of Civil Engineering and Architecture at Guangxi University, Nanning, China
27 530004, liangshilin@st.gxu.edu.cn

28 ³Assistant Professor, School of Civil Engineering, Southeast University, 2 Sipailou, Nanjing 210096,
29 China. Email: dcfeng@seu.edu.cn

30 ⁴Senior Lecturer in Structural Engineering, School of Mathematics, Computer Science and Engineering,
31 City, University of London, U.K., Feng.Fu.1@city.ac.uk

32 ⁵Professor, Key Laboratory of Concrete and Prestressed Concrete Structures of the Ministry of Education,
33 Southeast University, 2 Sipailou, Nanjing 210096, China. Email: g.wu@seu.edu.cn

34 **INTRODUCTION**

35 Due to the increasing terrorist activities recently, the likelihood of structures subjected to
36 extreme loads increased dramatically. After extreme loading, the structures may loss columns or
37 partial of walls, which may cause the shear force and bending moment of the adjacent structural
38 components increase significantly. For a structural frame designed primarily to resist gravity
39 load, the beams adjoining to the damage zone are hardly able to resist the extra bending moment
40 purely relied on their designed flexural strength, and prone to propagate the damage. This type of
41 collapse is called disproportionate collapse or progressive collapse. Progressive collapse first
42 caught the public attentions after the collapse of Ronan Point apartment in 1968. The collapse of
43 Murrah Federal building in 1995 and Twin Tower in World Trade Center in 2001 re-ignited the
44 upsurge for investigating the behavior of buildings to mitigate progressive collapse. Several
45 design guidelines (GSA 2003 and DoD 2009) are successively promulgated. Two main design
46 methods (indirect and direct design) are commonly accepted for evaluation of the progressive
47 collapse risks. For indirect design method, the minimum redundancy, integrity, ductility, and
48 tie-force is required. For direct design method, alternative load path method is commonly used
49 as it is threat independent. As mentioned above, fully relying on flexural strength may be not
50 enough to resist the propagation of damage. Therefore, it is necessary to pursue other possible
51 load resisting mechanisms, which are not evoked in normal building design. Studies (Sasani and
52 Kropelnicki 2008, Yi et al. 2008, Su et al. 2009, Orton et al. 2009, Sadek et al. 2011, Qian and Li

53 2013, Qian et al. 2015, Yu et al. 2017, Yu et al. 2019) were carried out to evaluate the reliability
54 of compressive arch action (CAA) and tensile catenary action (TCA) to enhance the load
55 resisting capacity of reinforced concrete (RC) frames. Qian and Li (2012), Qian and Li (2015),
56 Lu et al. (2017), and Ren et al. (2016) quantified the slab effects on load resisting capacity of RC
57 frames to mitigate progressive collapse. Orton and Kirby (2014), Qian and Li (2015), Peng et al.
58 (2017), Qian and Li (2017), and Qian et al. (2018) investigated the dynamic response of RC
59 beam-column substructures or flat slab substructures subjected to sudden column removal
60 scenarios. The dynamic increase factors caused by sudden column removal and residual strength
61 of the substructures after dynamic vibration are also evaluated and discussed. However, these
62 experimental works mainly focused on conventional RC frames while studies on precast
63 concrete (PC) frames were rare. Kang and Tan (2015, 2017) conducted two series of PC
64 beam-column substructures with cast-in-place monolithic joints subjected to the loss of a middle
65 column scenario. Moreover, Feng et al. (2019) simulated the behavior of PC frames to resist
66 progressive collapse. These studies found that PC frames with cast-in-place monolithic joints
67 performed similar behavior as conventional RC frames in terms of load resisting mechanism and
68 failure modes. Qian and Li (2019) tested three-dimensional PC beam-column-slab specimens
69 with monolithic joints to evaluate the behavior of PC frames subjected to a penultimate column
70 removal scenario. It was found that PC slabs achieved similar integrity as cast-in-situ slabs.
71 However, milder tensile membrane action could be mobilized due to discontinuous
72 reinforcements in slab. Lew et al. (2017) tested two full-scale PC beam-column sub-assemblages
73 with welded connection (dry connection) subjected to the loss of a middle column scenario. In
74 contrast with conventional RC beam-column sub-assemblages, no TCA was observed in these
75 PC specimens due to fracture of the anchorage bars at the welded connection. Qian and Li (2018)

76 tested a series of two PC and one RC beam-column-slab substructures subjected to a penultimate
77 column loss scenario. Two PC substructures had welded or bolted beam-to-column connections,
78 respectively. Similar to Lew et al. (2017), fracture of the anchorage studs at welded connection
79 (dry connection) prevented the beams to develop TCA. For the bolted connection (another type
80 of dry connection), the gap between the beam and column interfaces prevents the beams to
81 develop CAA while beam discontinuous longitudinal reinforcements prevents the development
82 of TCA in large deformation stage. The poor behavior of PC substructures with welded and
83 bolted connection requires looking for more robustness type of dry connection to resist
84 progressive collapse. Based on seismic evaluation, PC frames with post-tensioned connections
85 or called post-tensioned precast concrete (PTPC) system may be an alternate choice (Lu et al.
86 2019).

87 PTPC system was first proposed by Cheok and Lew (1991) as a portion of PREcast
88 Seismic Structural System (PRESSSS) program. Fig. 1 exhibits typical types of PTPC
89 connections: a) unbonded connection; b) partially bonded connection; and c) fully bonded
90 connection. In these connections, two strands pass through the beams and columns parallelly to
91 assemble them. Spiral hoops are embedded at the beam ends to enhance the concrete strength.
92 Before assembling, interfaces between the precast beams and columns are grouted. Seismic tests
93 (Cui et al 2017, Guo et al 2019) indicated that PTPC connection has favorable self-centering
94 ability. Fully bonded PTPC beam-column sub-assemblages performed comparable ductility as
95 monolithic RC sub-assemblages. However, as fully bonded PTPC sub-assemblages were prone
96 to develop inelastic strain in the post-tensioning tendons due to uneven distribution of stress. The
97 effective prestressing force in the tendons would reduce in large deformation stage and resulted
98 in the degradation of the ability of shear force transferred from beam to column. To overcome

99 these drawbacks, extensive studies were carried out on partially bonded or unbonded PTPC
100 beam-column sub-assemblages subjected to seismic loads experimentally. Priestley and Tao
101 (1993) discussed the lateral force-displacement characteristic of partially bonded PTPC
102 beam-column sub-assemblages subjected to seismic loads. Stanton et al. (1997) tested a series of
103 partially bonded PTPC beam-column sub-assemblages with bonded reinforcements at the top
104 and bottom of the beam ends. They found that the hybrid system (post-tensioned tendons and
105 mild reinforcements) could achieve similar flexural strength as conventional RC system even
106 with similar member size. The shear resistance of the hybrid system was superior to that of
107 conventional RC system as no degradation of the shear strength was observed during test.
108 Similar conclusions were found in Stone et al. (1995) based on additional specimens with
109 advanced hybrid system.

110 Based on above investigations, the advantages of PTPC beam-column sub-assemblages,
111 especially unbonded ones, were summarized as below. If it is designed properly, the
112 post-tensioned tendons will remain elastic at required ultimate displacement. Thus, no prestress
113 force loss would be resulted after unloading from the design level of ductility. Consequently, no
114 degradation of shear friction at beam-column interface occurred. The beam and column elements
115 would only have elastic response and little damage. The PTPC connection has self-centering
116 ability, which means the connections could return to its original equilibrium position without any
117 residual deflection. Although PTPC has so many advantages, few studies were carried out on
118 their progressive collapse resistance. Due to its special configuration of connections, the load
119 resisting mechanisms of PTPC frames are expected to be quite different to that of conventional
120 RC frames and normal PC frames with welded or bolted connection. To fill this gap, in this
121 paper, a series of four unbonded PTPC beam-column sub-assemblages were designed and tested.

122 The load resisting mechanisms of this type of structure were investigated in detail. Relevant
123 design recommendations were also made.

124 **Experimental Program**

125 Figs. 2(a) and (b) illustrate the bending moment diagram of a frame subjected to the loss of
126 an interior and penultimate column, respectively. As shown in the figure, bending moment
127 reverse was observed at the middle joint. Moreover, the negative bending moment at the side
128 joints were increased significantly after removal of the column. Therefore, the sub-assemblages
129 just above the removed column are the key components in the entire frame, as highlighted in
130 Figs. 2(a) and (b). To well reflect the structural mechanisms of the frame, a sub-assemblage
131 consisted of a double-span beam, two overhanging beams, two side columns, and one interior
132 column stub was extracted from a multi-story frame at the inflection points of the bending
133 moment diagram, as illustrated in Fig. 2(a). As shown in Fig. 2(b), for the frame subjected to the
134 loss of a penultimate column scenario, no overhanging beams were designed as the horizontal
135 constraints were mainly controlled by the side column without overhanging beam.

136 *Specimen Design*

137 Four 1/2 scaled specimens (UPI-0.4, UPI-0.65, UPE-0.4, and UPE-0.65) were tested in this
138 study, as tabulated in Table 1. The prototype building is an eight-storey frame, which was
139 designed in accordance with ACI 318-14 (2014). The prototype frame was located on a D class
140 site. The design spectral acceleration parameters of S_{DS} and S_{D1} are 0.46 and 0.29, respectively.
141 The design live load of the prototype frame is 2.0 kPa. The dead load including the ceiling
142 weight is 5.1 kPa.

143 The specimens are named as follows: for an example, UPI-0.4 denotes a PTPC specimen,
144 which has effective prestress of $0.4f_{pu}$ in tendons, subjected to the loss of an interior column

145 scenario. Note that f_{pu} represents the ultimate strength of prestressing tendons. Fig. 3 illustrates
146 the dimensions and reinforcement details of tested specimens. All specimens have identical
147 dimensions and reinforcement details. The difference between UPE and UPI series specimens
148 was whether having overhanging beams. As shown in the figure, the cross section of the beam
149 and column is 150 mm×250 mm and 250 mm×250 mm, respectively. For the purpose to install
150 tendons in assembly stage, two PVC ducts with diameter of 20 mm were pre-embedded in PC
151 members before casting. The PC beam was reinforced by 2T12 at both top and bottom layer with
152 reinforcement ratio of 0.66 %. As the longitudinal reinforcements did not pass through the joints,
153 they were bent up to 90 degrees hook with tail of 170 mm (larger than $12d_b$). Note that, d_b
154 represents diameter of reinforcement. The design span of the beam was 3000 mm and thus, the
155 span/depth ratio was 12. Two prestressing tendons with diameter of 12.7 mm and nominal area
156 of 98.7 mm² were positioned in ducts in the two-span beams, side columns, and overhanging
157 beams (if any), and were anchored for resisting the gravity and seismic load induced shear force.
158 A steel plate with thickness of 20 mm was placed at jacking end of each tendon. Moreover, spiral
159 hoops with diameter of 60 mm and pitch of 8 mm were installed at the beam ends to further
160 enhance the compressive strength of concrete. For UPE-0.4 and UPI-0.4, effective prestress of
161 $0.4f_{pu}$ was designed as larger deformation ability was preferred and the fracture of tendons
162 should be prevented in required deformation stage (Chock and Lew 1991). The only difference
163 between UPE-0.65 and UPE-0.4 was higher effective prestress of $0.65f_{pu}$ designed. As shown in
164 Fig. 3, before post-tensioning, 15 mm wide construction gap between beam and column
165 interfaces was filled by high strength grout (measured compressive strength about 50 MPa). To
166 reduce the loss of prestressing force, the specimens were tested 24 hours after jacking.

167 ***Material Properties***

168 Based on compressive and split cylinder concrete tests, the compressive strength and
169 splitting tensile strength at the day of test was 40.0 MPa and 3.7 MPa, respectively. The
170 properties of reinforcing bar and prestressing tendons were tabulated in Table 2.

171 ***Test Setup and Instrumentation***

172 Fig. 4 illustrates the test setup and instrumentations layout of UPI-series specimens, which
173 are similar to Yu and Tan (2017). Relied on the position of inflection points, the column height
174 and length of overhanging beam were determined. Thus, pin support was applied at the bottom
175 of each side column. To exam the effects of axial compressive force at the side column, the
176 column top was supported by a roller, rather than a pin. As shown in Fig. 4(a), another horizontal
177 roller was connected to the overhanging beam to replicate the horizontal constraints from
178 surrounding bays. The axial compressive force ($0.2f'_cA_g$, where f'_c is the compressive
179 cylinder strength and A_g is the sectional area) was applied on the side column by a hydraulic
180 jack (Item 4 in Fig. 4(a)) with a load capacity of 2000 kN and a commonly used self-equilibrium
181 system (based on two 50 mm thick steel plates and four 50 mm diameter bolts). The interior or
182 penultimate column was removed before applying the vertical load, which was applied by a
183 hydraulic jack (Item 1 in Fig. 4(a)). To prevent undesired out-of-plane failure, a specially
184 designed steel assembly (Item 3 in Fig. 4(a)) was installed underneath the jack. For UPE series,
185 no overhanging beams were designed at both sides as the loss of a penultimate column was
186 assumed. In reality, as shown in Fig. 2(b), overhanging beam should be included at one of the
187 side columns to reflect the reality more accurate. However, as pointed by Yu and Tan (2017), for
188 the scenario of loss of a penultimate column, the extent of horizontal constraints was controlled
189 by the side column without overhanging beam. As shown in Fig. 3(c), for UPE series, the

190 horizontal constraints were only provided by the top roller and bottom pin support. To monitor
191 the behavior of specimens, a series of load cells, linear variable displacement transducers
192 (LVDTs), and strain gauges were installed externally or internally. The applied vertical load was
193 measured by a load cell (Item 2 in Fig. 4(a)) just beneath the jack. The axial force of the roller
194 installed horizontally was measured by the tension/compression load cell (Item 5 in Fig. 4(a)).
195 The horizontal and vertical reaction force at the bottom pin connection was measured by the
196 specially ordered load pin (Item 8 in Fig. 4(a)), which could measure the horizontal and vertical
197 reaction force explicitly. The variation of prestress force in the tendon was monitored by two
198 load cells (Item 7 in Fig. 4(a)). The axial force applied at the side column was monitored by the
199 reading of oil pump for the jack (Item 4 in Fig. 4(a)). A series of LVDTs were installed along the
200 beams and side columns to monitor the deformation of the beams and columns at different
201 loading stages. A series of strain gauges were mounted at beam reinforcements to measure the
202 varying of local strain in reinforcing bars during tests.

203 **Test Results**

204 Four PTPC beam-column sub-assemblages were tested by push-down loading procedure to
205 investigate the behavior of unbonded PTPC frames to resist progressive collapse caused by
206 different column removal scenarios. Main results were tabulated in Table 3 and discussed as
207 below.

208 *Global Behavior and Failure Modes*

209 *UPE Series*

210 UPE-0.4 and UPE-0.65, which are subjected to the loss of a penultimate column scenario,
211 have effective prestress (f_{pe}) of $0.4f_{pu}$ and $0.65f_{pu}$, respectively. Fig. 5 shows the applied
212 load-vertical displacement relationship of the specimens. When the vertical displacement of

213 middle joint (MJD) reached 45 mm and 39 mm, respectively, first peak load of 30 kN and 39 kN
214 were measured for UPE-0.4 and UPE-0.65, respectively, which indicates the specimen with
215 higher effective prestress achieved higher compressive arch action (CAA) capacity due to higher
216 pre-compressive stress in concrete. Further increasing the MJD to 246 mm, the load resistance of
217 UPE-0.4 exceeds that of UPE-0.65 until the end of test. This is because that the specimen with
218 higher effective prestress (UPE-0.65) suffered greater shear and bending moment demands for
219 side columns as well as greater $P-\Delta$ effects, which leads to earlier strength and stiffness
220 degradation. Further increasing MJD, wider cracks or opening occurred at beam-column
221 interfaces and accompanied by concrete crushing at the compression toes. At MJD of 315 mm
222 and 270 mm, flexural cracks were also observed at the side columns of UPE-0.4 and UPE-0.65,
223 respectively. The ultimate load capacity of 66 kN was obtained at an MJD of 440 mm for
224 UPE-0.65. At this loading stage, obvious inward lateral movements were observed at right
225 column. Concrete crushing occurred at the outer side of the right column. Further increasing
226 MJD, the failure of the side column became more severe and the load resistant capacity kept
227 decreasing. The test of UPE-0.65 was stopped at an MJD of 599 mm due to severe damage
228 occurred in the side columns. For UPE-0.4, the ultimate load capacity of 73 kN was obtained at
229 an MJD of 540 mm. After that, the load resistance kept decreasing with further increasing the
230 displacement. The failure modes of UPE-0.4 and UPE-0.65 were illustrated in Figs. 6 and 7,
231 respectively.

232 As shown in the figures, the failure modes of UPE-0.4 and UPE-0.65 were quite similar. No
233 cracks were observed along the whole beam span. This is quite different to conventional RC
234 sub-assemblages (Yu and Tan 2017). In their tests, plastic hinges were formed at the beam ends.
235 In TCA stage, full-depth penetrated flexural cracks formed along the beam as the tensile force in

236 RC sub-assemblages was provided by continual longitudinal reinforcements, rather than the
237 unbonded prestressing tendons. For UPE series specimen, concrete crushing occurred in the
238 beam's compression toes with wide openings observed at beam-column interfaces regions. For
239 UPE-0.65, the maximum opening width of 48 mm and 41 mm were measured at the middle
240 column and side column interfaces, respectively. For right column, wide flexural cracks were
241 observed at the inner face and severe concrete crushing occurred at the outer face, which is a
242 typical large eccentric compression failure due to the combined action of lateral tensile force and
243 vertical axial force. However, the left side column experienced narrower flexural cracks as the
244 damage prone to concentrated in one side (relatively weak) although both sides have similar
245 dimensions and reinforcement details.

246 *UPI Series*

247 UPI-0.4 has effective prestress of $0.4f_{pu}$. In addition, this specimen subjected to an
248 interior-column-removal scenario and both side columns have overhanging beams. As shown in
249 Fig. 4a, a roller support was applied at each overhanging beam to provide horizontal constraints
250 and thus, compared to UPE-0.4 which has no overhanging beam, UPI-0.4 has a much stronger
251 horizontal constraint at boundary. When MJD reached 10 mm, flexural crack or opening was
252 observed in the beam-column interfaces. When the MJD reached 29 mm, the first peak load of
253 35 kN, which was 116.6 % of that of UPE-0.4, was measured. Further increase MJD to 110 mm,
254 slight concrete crushing occurred at the middle column-beam interfaces. The flexural cracks first
255 occurred at the right column at an MJD of 320 mm. Further increasing MJD, the opening at the
256 beam-column interfaces became wider. With the increase of MJD to 631 mm, the fracture of one
257 wire at the bottom tendon resulted in a sudden drop of load resistance. And the maximum
258 opening width of 57 mm and 67 mm were measured at the middle column and side column

259 interfaces, respectively. After that, the load resistance kept increasing with increase of MJD. The
260 test was stopped at an MJD of 652 mm corresponding to the ultimate load capacity of 151 kN as
261 the hydraulic jack reached its stroke capacity. The failure mode of UPI-0.4 is shown in Fig. 8.
262 Wide opening with width about 60 mm was measured at the beam-middle column interface. For
263 beam-side column interfaces, the beam and column were fully lost contact and only connected
264 by tendons. Different to UPE-0.4, the cracks at the side columns were much thinner and no
265 concrete crushing was observed.

266 Comparing to UPI-0.4, UPI-0.65 has higher effective prestress of $0.65 f_{pu}$. The first peak
267 load of 44 kN, which was 125.7 % of that of UPI-0.4, was measured at an MJD of 39 mm. As
268 shown in Fig. 5, the load resistance of UPI-0.65 is slightly higher than that of UPI-0.4 before
269 MJD reached 303 mm due to higher effective prestress clamping the specimen tighter and
270 greater compressive arch action was mobilized. The concrete crushing was first observed at the
271 beam-middle column interface at an MJD of 70 mm which was earlier than that of UPI-0.4. The
272 crack occurred at the side column at an MJD of 300 mm, which was also earlier than that of
273 UPI-0.4. The ultimate load of 131 kN was obtained at an MJD of 542 mm. At this stage, some
274 wires of the tendon were ruptured, and the load resistance suddenly dropped. Further increasing
275 MJD, the load resistance almost kept constant. At an MJD of 628 mm, both tendons were
276 fractured and the MJD suddenly increased to 641 mm with the loss of load resistance. And the
277 maximum opening width of 55 mm and 60 mm were measured at the middle column and side
278 column interfaces, respectively. The failure mode of UPI-0.65 was shown in Fig. 9. In general, it
279 was very similar to that of UPI-0.4, except both tendons were fractured.

280 ***Horizontal Reaction Force***

281 Fig. 10 shows the contribution of horizontal restraints to the total horizontal reaction at

282 right side. Negative values represent compressive force while positive values mean tensile force.
283 As shown in Fig. 10(a), for UPE-0.65, at small deformation stage, the compressive reaction
284 force mainly attributed into bottom pin connection. However, at large deformation stage, the
285 tensile force is equally from top and bottom supports. Different to UPE-0.65, as shown in Fig.
286 10(b), the tensile reaction force of UPI-0.65 kept almost constant after MJD beyond 478 mm due
287 to yielding of prestressing tendons. The drop of reaction force at MJD of 542 mm and 628 mm
288 was due to the fracture of tendons suddenly.

289 *Deformation of Beams and Columns*

290 The deformation shape of double-span beams of UPI-0.4 is plotted in Fig. 11. It was found
291 that the beam kept almost straightly during the test, which agreed well with the observations that
292 no plastic hinges were formed at the beam ends. In general, similar phenomena were observed
293 for all specimens. Fig. 12(a) shows the drift profile of side column of UPI-0.65. As shown in the
294 figure, the column initially deformed outward (refer to negative value) with maximum outward
295 movement of 0.5 mm at MJD of 100 mm, which was caused by compressive forces developed in
296 the beams. Further increasing the MJD to 300 mm, the side column returned to its initial position.
297 After that, inward movement was observed. The maximum inward movement of 5.1 mm was
298 recorded at MJD of 500 mm due to catenary action developed by prestressing tendons and P- Δ
299 effects. It should be noted that overhanging beams were designed beyond the side column. Fig.
300 12(b) illustrates the drift profile of right column of UPE-0.65. Similar to UPI-0.65, the maximum
301 outward movement of 0.8 mm was measured at MJD of 100 mm. Then, the side column began
302 to move inward. When the MJD reached 500 mm, the maximum inward movement of 48.1 mm
303 was recorded at the beam axis. The larger inward movement in UPE-0.65 was mainly due to
304 absence of overhanging beams, which resulted in less horizontal constraints for beams.

305 Moreover, when side column experienced large inward movements, the P- Δ effects due to
306 applied axial force would aggravate the damage of side column and further increased the inward
307 movements. The maximum inward and outward movements of the right column of UPE-0.4
308 were 0.6 mm and 39.9 mm, which were slightly less than that of UPE-0.65. Fig. 13 illustrates the
309 relationship of total horizontal reaction versus horizontal drift at the center of beam-side column
310 joint. At small deformation stage, the slopes (i.e., horizontal stiffness) of the curves are similar.
311 However, the slopes of UPI series are much larger than that of UPE series at large deformation
312 stage due to considerable constraint provided by the overhanging beams.

313 *Strain Gauge Reading*

314 Figs. 14 and 15 show the strain distribution along longitudinal reinforcement of typical
315 specimens. For UPI-0.65, as shown in Fig. 14(a), compressive strain about $-280 \mu\epsilon$ was recorded
316 in bottom longitudinal reinforcements after anchoring the tendons. However, when MJD reached
317 20 mm, some of the measuring point near the interface of middle column reduced to $0 \mu\epsilon$ due to
318 wide opening occurred there. With further increase of MJD up to 250 mm, the compressive
319 strain kept increasing especially for points close to the side column.

320 However, further increasing the MJD to 500 mm, the compressive strain close to the side
321 column began to reduce as entire section between beam and side column began to separate. For
322 top rebar, as shown in Fig. 14(b), compressive strain about $-280 \mu\epsilon$ was also recorded.
323 Conversely, the strain near the side column dropped to $0 \mu\epsilon$ at MJD of 20 mm due to wide
324 opening. Similarly, when MJD reached 500 mm, the strain along whole top rebar began to
325 decrease because entire section between beam and side column began to loss contact or full
326 depth opening. For UPI-0.4, similar results were recorded. The strain along the whole bottom
327 and top rebar almost reduced to $0 \mu\epsilon$ at the MJD of 500 mm due to the opening between the

328 beam and side column interfaces was wider. For UPE-0.65, as shown in Fig. 15, similar results
329 were observed before the MJD reached 250 mm. However, when MJD achieved 500 mm, the
330 compressive strain at the interfaces between beam and column kept increasing, rather than
331 decreasing. This could be attributed to the large lateral deformation of the side columns allowing
332 the beam and column to keep contact in compressive zone. Similar results were measured for
333 UPE-0.4.

334 *Variation of Prestressing Force in Tendons*

335 Fig. 16 illustrates the various prestressing force in tendons with the increase of MJD. As
336 shown in the figure, after post-tensioning, the total prestressing force of tendons in UPI-0.65,
337 UPI-0.4, UPE-0.4, and UPE-0.65 were 237 kN, 150 kN, 153 kN, and 239 kN, respectively. The
338 measured maximum force of the tendons was 329 kN, 323 kN, 269 kN, and 307 kN, respectively.
339 Thus, only the tendons in UPI series were yielded. Comparing to UPI-0.65, the increase of
340 prestressing force in tendons of UPI-0.4 was much faster. The tendons in UPI-0.65 were yielded
341 at MJD of 322 mm, which was much earlier than that of UPI-0.4 (at MJD of 541 mm).

342 **Discussion of the Results**

343 *The Effects of Effective Prestress*

344 As shown in Fig. 5 and Table 3, the first peak load of UPE-0.4, UPE-0.65, UPI-0.4, and
345 UPI-0.65 were 30 kN, 39 kN, 35 kN, and 44 kN, respectively. Thus, higher effective prestress
346 could increase the first peak load by 30.0 % and 25.7 % for UPE and UPI series, respectively.
347 Moreover, the ultimate load capacity of UPE-0.4, UPE-0.65, UPI-0.4, and UPI-0.65 were 73 kN,
348 66 kN, 151 kN, and 131 kN, respectively. Therefore, the higher effective prestress might
349 aggravate the damage of side column of UPE series specimens and resulted in less ultimate load
350 capacity. As shown in Figs. 7 and 8, the higher effective prestress resulted in the tendons of

351 UPI-0.65 began to fracture at MJD of 542 mm, which was much earlier than that of UPI-0.4.
352 Therefore, in general, lower effective prestress was preferred for PTPC frame to resist
353 progressive collapse. Actually, similar suggestion was given by Cheok and Lew (1991) for
354 seismic resisting design.

355 *The Effects of Boundary Conditions*

356 As shown in Table 3 and Fig. 5, comparing with UPE series specimens, UPI series
357 specimens increased the first peak load and ultimate load capacity up by 16.7 % and 106.8 %,
358 respectively. Therefore, stronger horizontal constraints might not increase the first peak load
359 significantly. However, stronger horizontal constraints did enhance the ultimate load capacity at
360 large deformation stage effectively. This is because the stronger horizontal constraints allowed
361 full exploitation of the tendons at large deformation stage. Regarding failure modes, the failure
362 of UPE series specimens was controlled by the large eccentric compression failure of the side
363 column. However, the failure of UPI series specimens was controlled by the fracture of tendons.

364 *Dynamic Resistance of Specimens*

365 It is worth to note that progressive collapse normally is a dynamic problem. In other words,
366 the column removal is generally in a sudden manner and thus, it is necessary to evaluate the
367 dynamic resistance of the tested specimens via energy method proposed by Izzuddin et al. (2008).
368 In their method, the external work was assumed to equal the strain energy stored in the frame
369 when the kinetic energy was decreased to zero. Thus, the dynamic resistance of the specimens
370 could be determined by Eq. (1).

$$371 \quad P_d = \frac{1}{u_d} \int_0^{u_d} P(u) du \quad (1)$$

372 where P_d and $P(u)$ represent the pseudo-static resistance and the quasi-static resistance at the
373 displacement demand u_d , respectively.

374 Fig. 17 illustrates the behavior of dynamic resistance of the tested specimens. The
 375 measured maximum dynamic ultimate load capacity of UPI-0.4, UPI-0.65, UPE-0.4, and
 376 UPE-0.65 were 71 kN, 67 kN, 49 kN, and 47 kN, respectively. Similar to the conclusions from
 377 non-linear quasi-static tests, the specimens with stronger horizontal constraints achieved larger
 378 dynamic ultimate load capacity. The specimens with lower effective prestress in tendons
 379 performed better. In DoD (2009), the dynamic increase factor (DIF) could be determined for RC
 380 frames by Eq. 2.

$$381 \quad D I F = 1 + 0.4 \frac{\sigma_p}{f_a} \left(\frac{\theta_{pra}}{\theta_y} \right) \quad (2)$$

382 where θ_{pra} is the plastic rotation for collapse prevention; θ_y is the rotation at yield.

383 It should be noted that for PTPC frame, beam reinforcements were not yielded during test
 384 and thus, Eq. 2 is not suit for PTPC frames. In the future, more dynamic tests and analysis should
 385 be carried out to give equation for predicting DIF of PTPC frame and to refine the design guideline
 386 (DoD 2009).

387 ***Variation of Bending Moment in Side Column of UPE specimens***

388 The varying of bending moment of the side column of UPE specimens were determined by
 389 measured reaction forces to deep understand the failure mode of side columns of UPE specimens.
 390 Fig. 18 illustrates the force equilibrium diagram of the side column. The bending moment in
 391 section E-E can be determined by Eq. (3):

$$392 \quad M_E = H_l l_0 + V_l \Delta \quad (3)$$

393 where H_l is horizontal reaction in top horizontal constraint; l_0 is distance from top
 394 horizontal constraint to section E-E; V_l is axial compression on side column; and Δ is horizontal
 395 movement in section E-E.

396 As shown in Fig. 18, the bending moment was negative (clockwise direction) at small

397 deformation stage whereas positive (counter-clockwise direction) bending moment was
398 measured at large deformation stage. Compared to the negative bending moment, the positive
399 one was much larger. The maximum positive bending moments of UPE-0.4 and UPE-0.65 were
400 83.6 kN·m and 85.2 kN·m, respectively. Fig. 19 gives the theoretical bending moment-axial
401 force relationship curve of E-E section. As shown in the figure, the maximum bending moments
402 in E-E section of UPE specimens reached tension failure (large eccentric compression failure),
403 which agreed with the failure mode well.

404 *Discussion of Load Resisting Mechanisms*

405 As shown in Figs. 20 and 21, the load resisting mechanism of PTPC frames were
406 different with conventional RC frames (Yu and Tan 2017) or PC frames with monolithic joints
407 (Kang and Tan 2017). For conventional RC frames, the first onset load resisting mechanism is
408 flexural action. Further increasing the displacement, if the beam ends have sufficient horizontal
409 constraints, compressive arch action (CAA) may be triggered as the change of neutral axis may
410 result in the beam end moved outward, which was restrained by, as shown in Fig. 20(a). It is
411 vanished when concrete crushing occurred at the compressive zone. When the beams deformed
412 over one-beam depth, penetrated deep cracks occurred at the beams and the concrete stops to
413 contribute. Therefore, the load resistance is mainly attributed to the tensile force from beam
414 reinforcements, which is called tensile catenary action (TCA), as shown in Fig. 20(b).

415 However, for PTPC frames, no beam reinforcements passed through the joints and the
416 post-tensioning tendons are unbonded. Thus, no beam action is mobilized to resist progressive
417 collapse. As shown in Fig. 21(a), the concrete suffered considerable initial pre-compressive
418 stress due to post-tensioning. When the beams deformed, the rotation of the beam ends increased
419 the compressive stress in the compressive zone and CAA is developed. However, it should be

420 emphasized that the cause of CAA in PTPC frame is different to that in RC frame. In PTPC
421 frames, the CAA is actively applied due to post-tensioning tendons and thus, it will not vanish
422 even concrete is crushed. Moreover, as the CAA in PTPC will keep working as long as the beam
423 and column are still in contact and pre-compressive stress maintained. From this, when the MJD
424 beyond one-beam depth, the contribution of CAA in PTPC became negative, as shown in Fig.
425 21(b). Furthermore, different to RC frames, the TCA of tendons is mobilized from the beginning
426 of the test.

427 **Finite Element Analysis**

428 LS-DYNA (Hallquist 2008) was employed to develop a high fidelity finite element (FE)
429 models to deep understand the test results and to quantify the effects of loading method and
430 specimen design.

431 *Establishment of FE Model*

432 The concrete was modeled by an 8-node solid element with a reduced integration strategy.
433 Reinforcements were modeled by a 2-node Belytschko-Schwer beam element. Unbonded tendon
434 was modeled by 2-node spotweld beam. As shown in Fig. 22, a series of springs (relied on
435 element Combin 165) were horizontally connected to the top of side column and overhanging
436 beam (if any) to simulate the horizontal restraints while the bottom pin connection was modeled
437 by keyword *CONSTRAINED_JOINT_REVOLUTE. Continuous surface cap model (CSCM)
438 was used for concrete material due to its stability and accuracy (Yu et al. 2018, Yu et al. 2019). A
439 bilinear elastic-plastic model *MAT_PLASTIC_KINEMATIC was used for reinforcements. The
440 unbonded tendon was modelled by *MAT_SPOTWELD with proper definition of
441 *INITIAL_AXIAL_FORCE_BEAM. As suggested by previous studies (Yu et al. 2018, Weng et
442 al. 2019), perfect bond between reinforcement and concrete was assumed relied on *

443 CONSTRAINED_LAGRANGE_IN_SOLID. The beam elements of tendon were embedded into
444 concrete solid element by using *CONSTRAINED_BEAM_IN_SOLID whereas the constraint
445 along the beam axis was released to consider unbonded feature between the tendon and concrete.
446 *CONTACT_AUTOMATIC_SINGLE_SURFACE was defined well to simulate the interfaces
447 between the beam and column surfaces. As shown in Fig. 23, based on sensitivity analysis, the
448 beam ends with length of 100 mm from beam-column interface was meshed with size of 12.5
449 mm. However, the remaining regions were meshed with size of 25 mm because further mesh
450 refining would not enhance the accuracy but increase the computational time significantly.

451 *FE Model Validations*

452 Figs. 24 and 25 illustrate the failure modes of UPE-0.65 and UPI-0.65. Comparing with Figs. 7
453 and 9, it was found that the openings at the beam-column interfaces, concrete crushing at the
454 beam compressive toes, and cracks at side columns could be simulated well. However, for
455 UPE-0.65, its left-side column achieved more severe damage than the right-side column, which
456 was quite different with that from test observations. This could be explained that the damage will
457 concentrate at one of side columns when first crack occurred there, which was random in reality.
458 The failure mode of UPE-0.4 and UPI-0.4 was also well simulated. However, for the sake of
459 brief, the failure mode of UPE-0.4 and UPI-0.4 was not presented herein.

460 Fig. 26 compares the vertical load-displacement curves while Fig. 27 compares horizontal
461 reaction force-displacement curves. As shown in the figures, in general, the FE models could
462 reproduce the vertical load-displacement curves and horizontal reaction force-displacement
463 curves well. Therefore, the validated FE models were well validated and utilized to deeply
464 understand the test results and to investigate the effects of parameters excluded in experimental
465 program.

466 *Effect of Concrete Compressive Strength*

467 Fig. 28 shows vertical load-displacement curves of UPE-0.65 and UPI-0.65 with different
468 concrete strength. The FPL of UPE-0.65 increased from 41 kN to 46 kN when the concrete
469 compressive strength increased from 30 MPa to 50 MPa. Moreover, the UL increases from 75
470 kN to 83 kN as the higher concrete compressive strength increased lateral stiffness of the side
471 columns. For UPI-0.65, its FPL increased from 43 kN to 48 kN when the concrete compressive
472 strength increased from 30 MPa to 50 MPa while its UL decreased from 159 kN to 149 kN as the
473 higher concrete strength increased the stiffness of the side column which reduced the
474 deformation capacity of the specimen slightly.

475 *Effect of Axial Compression Ratio on Side Column*

476 Fig. 29 illustrates the effects of axial compression ratio on load resistance of UPE-0.65 and
477 UPI-0.65. Fig. 29(a) indicated that the higher axial compression ratio on side columns has little
478 effects on FPL of UPE-0.65. However, the UL of UPE-0.65 increased from 58 kN to 85 kN
479 when the axial compression ratio increased from 0.0 to 0.4. This is because the higher axial
480 compression force enhanced the lateral stiffness of side column. For UPI-0.65, conversely,
481 higher axial compression force at side columns will decrease the UL in large deformation stage
482 as the higher axial compression force increased the lateral stiffness of the side column, which
483 leads to the tendon fractured earlier.

484 *Effect of Boundary Condition*

485 To further study the effect of boundary condition on the behavior of PTPC frame. A model
486 named UPP-0.65 with asymmetric boundary was built. Compared with UPE-0.65, UPP-0.65 has
487 one overhanging beam at the right side. As shown in Fig. 30, the left side column of UPP-0.65
488 suffered severe damage while the damage in right side column was milder. In general, as shown

489 in Fig. 31, the vertical load-displacement curve of UPP-0.65 was similar to that of UPE-0.65.
490 Therefore, the additional overhanging beam on the right side will not affect the behavior of
491 UPE-0.65 significantly since both UPP-0.65 and UPE-0.65 was failed due to large eccentric
492 compression failure of the side column without overhanging beam.

493 *Effect of Loading Method*

494 In this study, concentrated load (CL) was applied at the lost column to investigate the load
495 redistribution capacity of the specimens. However, gravity load is uniformly distributed along
496 the beams in reality. Thus, it is necessary to study the difference between these two loading
497 approaches. For this purpose, a multi-point load (ML) system was proposed in this numerical
498 analysis. As shown in Fig. 32, the ML system consists of three load transfer beams, four steel
499 plates, and a series of pin connections. Relying on the proposed ML system, the applied load can
500 be almost equally divided into four point loads. The positions of the four steel plates were
501 determined as shown in Fig. 33(a). As illustrated in Fig. 33(b), the ML system could produce
502 similar bending moment diagram as uniformly distributed load.

503 Figs. 34 and 35 show the failure mode of UPE-0.65 and UPI-0.65 under ML approach. It
504 was found that the beams did not keep straight, which was quite different from tested specimens.
505 Fig. 36(a) shows comparison of the vertical load-displacement curves of UPI-0.65 from ML and
506 CL approaches. It should be noted that the total load applied by ML approach should be divided
507 by two for equivalently comparing with that from CL approach. At the beginning, the load
508 resistance of UPI-0.65-ML (divided by two) was similar to that of UPI-0.65 measured from CL
509 approach. However, the deformation capacity of UPI-0.65-ML was much lower than that of
510 UPI-0.65-CL as the beams did not keep straight for UPI-0.65-ML. As shown in Fig. 36(b), the
511 load resistance of UPE-0.65-ML (divided by two) was similar to that of UPE-0.65-CL even at

512 large deformation stage. This is because the failure of UPE-0.65 was controlled by the eccentric
513 compression failure of the side column, rather than the fracture of the tendon. Similar results
514 were observed in UPE-0.4. Therefore, it was concluded that multi-point or uniformly distributed
515 load approach will not affect the failure mode and load resistance significantly, especially when
516 the loss of a penultimate column was considered.

517 **Conclusions**

518 In this study, a series of four post-tensioned precast concrete (PTPC) beam-column
519 sub-assemblages were tested under push-down loading procedure. Based on experimental results
520 and analysis, the main conclusions were drawn:

- 521 1. As an innovative PC construction type, test results indicated that PTPC frame has excellent
522 performance to mitigate progressive collapse. PTPC frame could develop desired large
523 deformation capacity and ultimate load capacity in large deformation stage.
- 524 2. The experimental results and analysis indicated that the load resisting mechanisms mobilized
525 in PTPC frames are quite different from conventional RC frames or PC frames with
526 monolithic joints. The compressive arch action (CAA) in PTPC was generated actively due
527 to pre-compressive stress by tendons. Thus, different to conventional RC frame, the
528 contribution of CAA in PTPC was negative when the vertical displacement beyond about
529 one-beam depth.
- 530 3. Different to RC frames, the tensile catenary action (TCA) by tendons is mobilized from the
531 beginning of the test. In RC frames, the CAA and TCA are mobilized in sequence. However,
532 in PTPC frames, the CAA and TCA are developed simultaneously from the beginning of the
533 test.
- 534 4. Higher effective prestress could enhance the first peak load of the frame as the higher

535 effective prestress increased the pre-compressive stress in concrete. However, the higher
536 effective prestress may also result in the fracture of tendons earlier and reduce its
537 deformation capacity and ultimate load capacity. Thus, for PTPC frames considering the
538 risks of progressive collapse, it is suggested to design effective prestress less than $0.65f_{pu}$.

539 5. Investigation on the effects of different column removal scenarios indicated that specimens
540 under the loss of an interior column performed best including the deformation capacity,
541 ultimate load capacity as well as first peak load capacity. This is because the overhanging
542 beams beyond the side columns could provide strong horizontal constraints to ensure the
543 tendon to fully develop its material properties. The failure of UPI series is controlled by
544 fracture of tendons. However, for UPE series, their failure was controlled by the large
545 eccentric compression failure of the side column.

546 6. Numerical results indicated that the concentrated loading approach may change the failure
547 mode and deformation capacity of the specimen, comparing to multi-point loading approach.
548 However, it will not affect the load resisting capacity of the specimen significantly.

549 **Data Availability**

550 Some or all data, models, or code generated or used during the study are available from the
551 corresponding author by request (list items).

552 **Acknowledgements**

553 This research was supported by a research grant provided by the Natural Science Foundation of
554 China (Nos. 51568004, 51868004). Any opinions, findings and conclusions expressed in this
555 paper are those of the writers and do not necessarily reflect the view of Natural Science
556 Foundation of China.

557 **REFERENCES**

- 558 ACI Committee 318. “Building Code Requirements for Structural Concrete (ACI 318-14) and
559 Commentary (318R-14).” American Concrete Institute, Farmington Hills, MI, 433 pp; 2014.
- 560 Cheok, G. S., and Lew, H. S. (1991). “Performance of Precast Concrete Beam-to-Column
561 Connections Subject to Cyclic Loading.” *PCI Journal*, 36(3): pp. 56-67.
- 562 DoD (2009). “Design of Building to Resist Progressive Collapse.” *Unified Facility Criteria*,
563 UFC 4-023-03, U.S. Department of Defense, Washington, DC.
- 564 Feng, D. C., Wang, Z., and Wu, G. (2019). “Progressive Collapse Performance Analysis of
565 Precast Reinforced Concrete Structures.” *Struct Design Tall Spec Build.*, 28(5): pp. e1612.
- 566 GSA (2003). “Progressive Collapse Analysis and Design Guidelines for New Federal Office
567 Buildings and Major Modernization Projects.” *U.S. General Service Administration*,
568 Washington, DC.
- 569 Guo, T., Hao, Y. W., Song, L. L., Cao, Z. L. (2019). “Shake-Table Tests and Numerical Analysis
570 of Self-Centering Prestressed Concrete Frame.” *ACI Structural Journal*, 116(3): pp. 3-17.
- 571 Hallquist, J. O. 2008. LS-DYNA, V. 971, keyword user’s manual. Livermore: Livermore
572 Software Technology Corporation
- 573 Kang, S. B., Tan, K. H., and Yang, E. H. (2015). “Progressive Collapse Resistance of Precast
574 Beam-Column Sub-assemblages with Engineered Cementitious Composites.” *Engineering
575 Structures*, 98: pp. 186-200.
- 576 Kang, S. B., and Tan, K. H. (2017). “Progressive Collapse Resistance of Precast Concrete
577 Frames with Discontinuous Reinforcement in the Joint.” *Journal of Structural Engineering*,
578 ASCE, 143(9), 04017090.
- 579 Lew, H. S., Main, J. A., Bao, Y. H., Sadek, F., Chiarito, V. P., Robert, S. D., and Torres, J. O.

580 (2017). "Performance of Precast Concrete Moment Frames subjected to Column Removal:
581 Part 1, Experimental Study." *PCI Journal*, 62(5): pp. 35-52

582 Cui, Y., Lu, X. L., Jiang C. (2017). "Experimental investigation of tri-axial self-centering
583 reinforced concrete frame structures through shaking table tests." *Engineering Structures*,
584 132: pp. 684-694.

585 Izzuddin, B. A., Vlassis, A. G., Elahazouli, A. Y., and Nethercot, D. A. (2008). "Progressive
586 Collapse of Multi-Story Buildings Due to Sudden Column Loss-Part 1: Simplified
587 Assessment Framework." *Engineering Structures*, 30(5): pp. 1308-1318.

588 Lu, X. Z., Lin, K. Q., Li, Y., Guan, H., Ren, P. Q., and Zhou, Y. L. (2017). "Experimental
589 Investigation of RC Beam-Slab Substructures against Progressive Collapse subjected to an
590 Edge-Column-Removal Scenario." *Engineering Structures*, 149: pp. 91-103.

591 Lu, X. Z., Lin, K., Gu, D., and Li Y. (2019). "Experimental Study of Novel Concrete Frames
592 Considering Earthquake and Progressive Collapse." *Concrete Structures in Earthquake*,
593 Springer, Singapore

594 Orton, S., Jirsa, O., J., and Bayrak, Q. (2009). "Carbon Fiber-Reinforced Polymer for Continuity
595 in Existing Reinforced Concrete Buildings Vulnerable to Collapse." *ACI Structural Journal*,
596 106(5): pp. 608–616.

597 Orton, S. L., and Kirby, J. E. (2014). "Dynamic Response of a RC Frame under Column
598 Removal." *Journal of Performance of Constructed Facilities*, 28(4): 04014010.

599 Peng, Z. H., Orton, S. L., Liu, J. R., and Tian, Y. (2017). "Experimental Study of Dynamic
600 Progressive Collapse in Flat-Plate Buildings Subjected to Exterior Column
601 Removal." *Journal of Structural Engineering*, 143(9): 04017125.

602 Priestley, M. J. N., and Tao, J. T. (1993). "Seismic Response of Precast Prestressed Concrete

603 Frames with Partially Debonded Tendon.” *PCI Journal*, 38(1): pp. 58-69.

604 Qian, K., and Li, B. (2012). "Slab Effects on Response of Reinforced Concrete Substructures
605 after Loss of Corner Column." *ACI Structural Journal*, 109 (6): pp. 845-855.

606 Qian, K. and Li, B. (2013). “Performance of Three-Dimensional Reinforced Concrete
607 Beam-Column Substructures under Loss of a Corner Column Scenario.” *Journal of
608 Structural Engineering*, ASCE, 139(4): pp.584-594.

609 Qian, K., and Li, B. (2015). "Quantification of Slab Influences on the Dynamic Performance of
610 RC Frames against Progressive Collapse." *Journal of Performance of Constructed Facilities*,
611 29(1):04014029.

612 Qian, K., Li, B., and Ma, J. X. (2015). "Load-Carrying Mechanism to Resist Progressive
613 Collapse of RC Buildings." *Journal of Structural Engineering*, ASCE, 141(2):
614 10.1061/(ASCE)ST.1943-541X.0001046, 04014107.

615 Qian, K., and Li, B. (2017). "Dynamic and Residual Behavior of Reinforced Concrete Floors
616 following Instantaneous Removal of a Column." *Engineering Structures*, 148: pp. 175-184.

617 Qian, K., and Li, B. (2018). “Performance of Precast Concrete Substructures with Dry
618 Connections to Resist Progressive Collapse.” *Journal of Performance of Constructed
619 Facilities*, ASCE, 32(2): 04018005.

620 Qian, K., Weng, Y. H., and Li, B. (2018). "Impact of Two Columns Missing on Dynamic
621 Response of RC Flat Slab Structures." *Engineering Structures*, 177: pp. 598-615.

622 Qian, K., and Li, B. (2019). "Investigation into Precast Concrete Floors against Progressive
623 Collapse." *ACI Structural Journal*, 116: pp. 171-182.

624 Ren, P. Q., Li, Y., Lu, X. Z., Guan, H., and Zhou, Y. L. (2016). "Experimental Investigation of
625 Progressive Collapse Resistance of One-Way Reinforced Concrete Beam-Slab Substructures

626 under a Middle-Column-Removal Scenario." *Engineering Structures*, 118: pp. 28-40.

627 Sasani, M. and Kropelnicki, J. (2008). "Progressive Collapse Analysis of an RC Structure." *The*
628 *Structural Design of Tall and Special Buildings*, 17(4): pp. 757-771.

629 Sadek, F., Main, J. A., Lew, H. S., and Bao, Y. H. (2011). "Testing and Analysis of Steel and
630 Concrete Beam-Column Assemblages under a Column Removal Scenario." *Journal of*
631 *Structural Engineering*, ASCE, 10.1061/(ASCE)ST.1943-541X .0000422, pp. 881–892.

632 Stanton, J., Stone, W. C., and Cheok, G. S. (1997). "A Hybrid Reinforced Precast Frame for
633 Seismic Regions." *PCI Journal*, 42(2): pp. 20-32.

634 Stone, W. C., Cheok, G. S., and Stanton, J. (1995). "Performance of Hybrid Moment-Resisting
635 Precast Beam-Column Concrete Connections Subjected to Cyclic Loading." *ACI Structural*
636 *Journal*, 92(2): pp. 229-249.

637 Su, Y. P., Tian, Y., and Song, X. S. (2009). "Progressive Collapse Resistance of
638 Axially-Restrained Frame Beams." *ACI Structural Journal*, 106(5): pp. 600-607.

639 Weng, Y. H., Qian, K., Fu, F., and Fang, Q. (2019). "Numerical Investigation on Load
640 Redistribution Capacity of Flat Slab Substructures to Resist Progressive Collapse." *Journal*
641 *of Building Engineering*, 101109.

642 Yi, W., He, Q., Xiao, Y., and Kunnath, S. K. (2008). "Experimental Study on Progressive
643 Collapse-Resistant Behavior of Reinforced Concrete Frame Structures." *ACI Structural*
644 *Journal*, 105(4): pp. 433-439.

645 Yu, J., and Tan, K. H. (2017). "Structural Behavior of Reinforced Concrete Frames Subjected to
646 Progressive Collapse." *ACI Structural Journal*, 114(1): pp.63–74.

647 Yu, J., Luo, L. Z., Li, Y. (2018). "Numerical Study of Progressive Collapse Resistance of RC
648 Beam-slab Substructures under Perimeter Column Removal Scenarios." *Engineering*

649 *Structures*, 159: pp.14–27.

650 Yu, J., Gan, Y. P., Wu, J., and Wu, H. (2019). “Effect of Concrete Masonry Infill Walls on
651 Progressive Collapse Performance of Reinforced Concrete Infilled Frames.” *Engineering*
652 *Structures*, 191: pp.179–193.

653

654 **Figure Captions**

655

656 **Fig. 1.** Typical PTPC connections: (a) unbonded connection; (b) partially bonded connection; (c)
657 fully bonded connection

658 **Fig. 2.** Bending moment diagram of a typical frame after column removal: (a) interior column
659 removal; (b) penultimate column removal

660 **Fig. 3.** Dimensions and reinforcement details of UPE-0.4 and UPI-0.4

661 **Fig. 4.** Test setup (a) photograph of UPI-series, (b) schematic view of UPI-series, and (c)
662 UPE-series

663 **Fig. 5.** Load-displacement relationships of test specimens

664 **Fig. 6.** Failure mode of specimen UPE-0.4

665 **Fig. 7.** Failure mode of specimen UPE-0.65

666 **Fig. 8.** Failure mode of specimen UPI-0.4

667 **Fig. 9.** Failure mode of specimen UPI-0.65

668 **Fig. 10.** Contribution of the horizontal reaction at right column: (a) UPE-0.65; (b) UPI-0.65

669 **Fig. 11.** Deformation shape of double-span beam in UPI-0.4

670 **Fig. 12.** Horizontal movements in side column: (a) UPI-0.65; (b) UPE-0.65

671 **Fig. 13.** The relationship of horizontal reaction force v.s. lateral drift at the center of beam-side
672 column joint

673 **Fig. 14.** Strain distribution along beam rebar of UPI-0.65: (a) bottom rebar; (b) top rebar

674 **Fig. 15.** Strain distribution along beam rebar of UPE-0.65: (a) bottom rebar; (b) top rebar

675 **Fig. 16.** Total prestressing force of tendons versus MJD

676 **Fig. 17.** Dynamic resistance of tested specimens

677 **Fig. 18.** The varying of bending moment in E-E section of side column

678 **Fig. 19.** Determination of the failure mode of UPE-series specimens

679 **Fig. 20.** Typical load resisting mechanisms in RC sub-assemblages: (a) compressive arch action;

680 (b) tensile catenary action

681 **Fig. 21.** Schematic view of load resisting mechanisms in PTPC sub-assemblages: (a) relatively

682 small deformation; (b) deformation larger than one-beam depth

683 **Fig. 22.** Geometrical model of UPI specimens

684 **Fig. 23.** Mesh size for beam end: (a) 8 mm; (b) 12.5 mm; (c) 25 mm

685 **Fig. 24.** Simulated mode of UPE-0.65

686 **Fig. 25.** Simulated failure mode of UPI-0.65

687 **Fig. 26.** Comparison of measured applied load-displacement curves with FE ones: (a) UPE-0.4

688 and UPI-0.4; (b) UPE-0.65 and UPI-0.65

689 **Fig. 27.** Comparison of measured horizontal reaction-displacement curves with FE ones: (a)

690 UPE-0.4 and UPI-0.4; (b) UPE-0.65 and UPI-0.65

691 **Fig. 28.** Effect of concrete strength on the resistance: (a) UPE-0.65; (b) UPI-0.65

692 **Fig. 29.** Effect of axial compression ratio on the resistance: (a) UPE-0.65; (b) UPI-0.65

693 **Fig. 30.** Simulated failure mode of UPP-0.65

694 **Fig. 31.** Comparison of applied load-displacement curves of UPE-0.65 and UPP-0.65

695 **Fig. 32.** Multipoint loading system

696 **Fig. 33.** Determination of loading point position: (a) loading approach; (b) bending moment

697 diagram

698 **Fig. 34.** Observation and failure mode of UPE-0.65 under ML approach

699 **Fig. 35.** Observation and failure mode of UPI-0.65 under ML approach

700 **Fig. 36.** Applied load-displacement curves of under different loading approaches: (a) UPI-0.65;
701 (b) UPE-0.65

702 **Table 1.** Specimen Properties

Test ID	Effective prestress	Axial compression ratio	Position of removed column	Span-to-depth ratio	Top and bottom beam longitudinal rebar ratio (%)	Overhanging beams
UPE-0.4	$0.4 f_{pu}$	0.2	Penultimate	12	0.66	NA
UPE-0.65	$0.65 f_{pu}$	0.2	Penultimate	12	0.66	NA
UPI-0.4	$0.4 f_{pu}$	0.2	Interior	12	0.66	Both sides
UPI-0.65	$0.65 f_{pu}$	0.2	Interior	12	0.66	Both sides

703 Note: f_{pu} is the nominal ultimate strength of the post-tensioning tendons (1860 MPa).

704

705 **Table 2.** Material Properties of Reinforcement and Post-tensioning Tendons

Item	Nominal diameter (mm)	Yield strength (MPa)	Ultimate strength (MPa)	Elastic modulus (GPa)	Elongation (%)
R6	6	368	485	162	20.1
T12	12	462	596	171	14.7
T16	16	466	604	182	17.0
Tendons	12.7	1649	1970	213	6.3

706 Note: R6 represents plain bar with diameter of 6 mm; T12 and T16 represent deformed rebar with diameter of 12
707 mm and 16 mm, respectively.

708

Table 3. Test Results

Test ID	MJD at FPL (mm)	MJD at UL (mm)	Resistance Re-ascending (mm)	FPL (kN)	UL (kN)	MHTF (kN)	MHCF (kN)
UPE-0.4	45	540	200	30	73	139	-66
UPE-0.65	39	440	230	39	66	139	-70
UPI-0.4	29	652	159	35	151	324	-96
UPI-0.65	39	542	201	44	131	328	-84

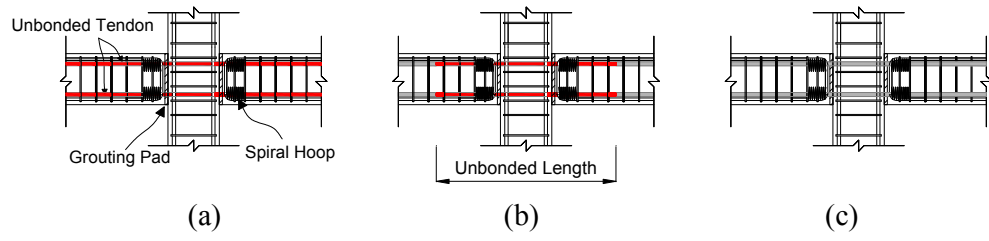
709 Note: MJD represents middle joint displacement; FPL and UL represent first peak load and ultimate load,
710 respectively; MHTF and MHCF represent maximum horizontal tensile force and maximum horizontal compressive
711 force, respectively.

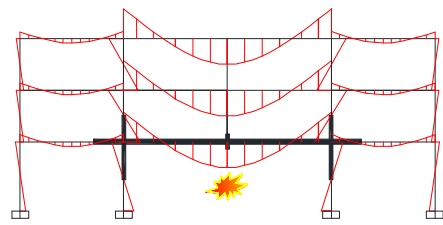
712

713

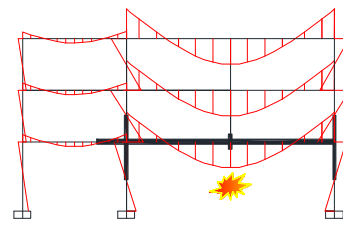
714

715

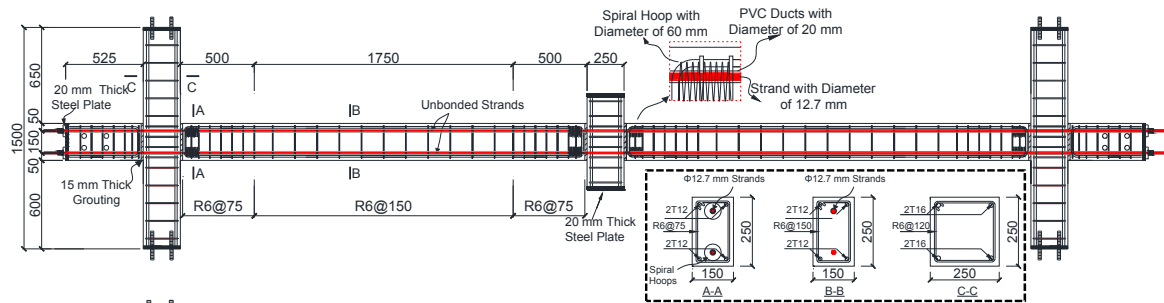




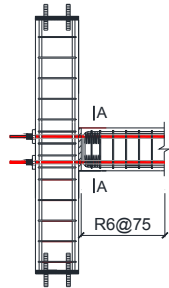
(a)



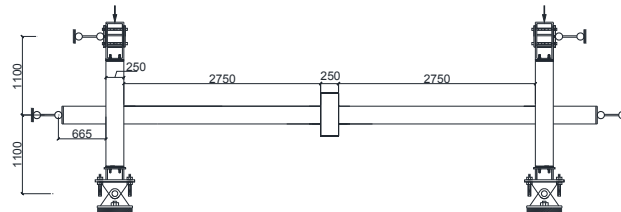
(b)



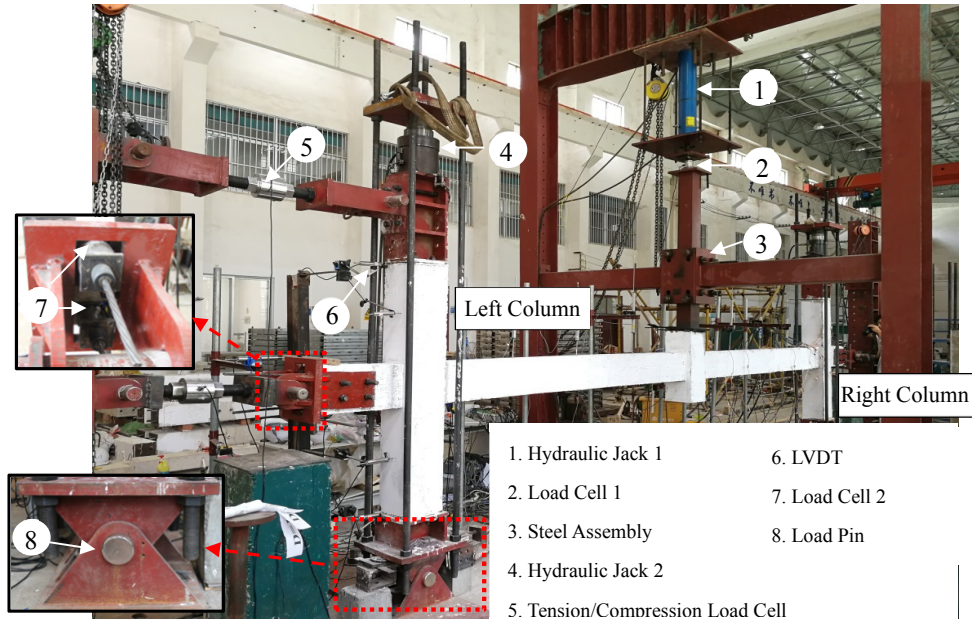
(a) Detailing of UPI-0.4



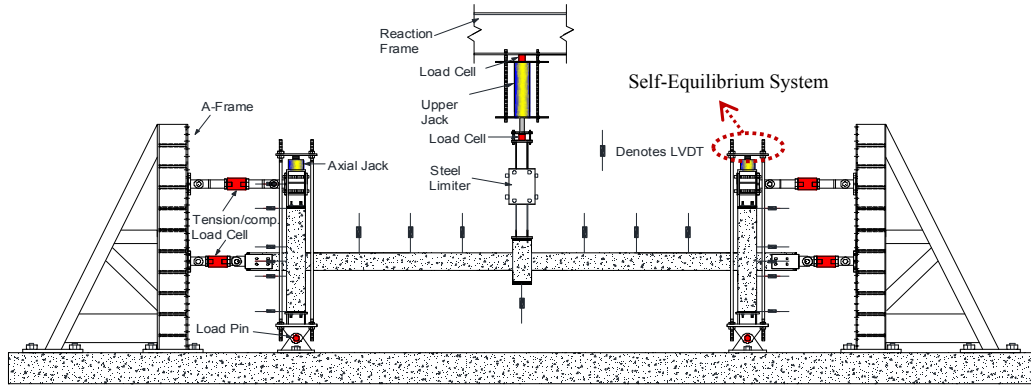
(b) Exterior joint detailing of UPE-0.4



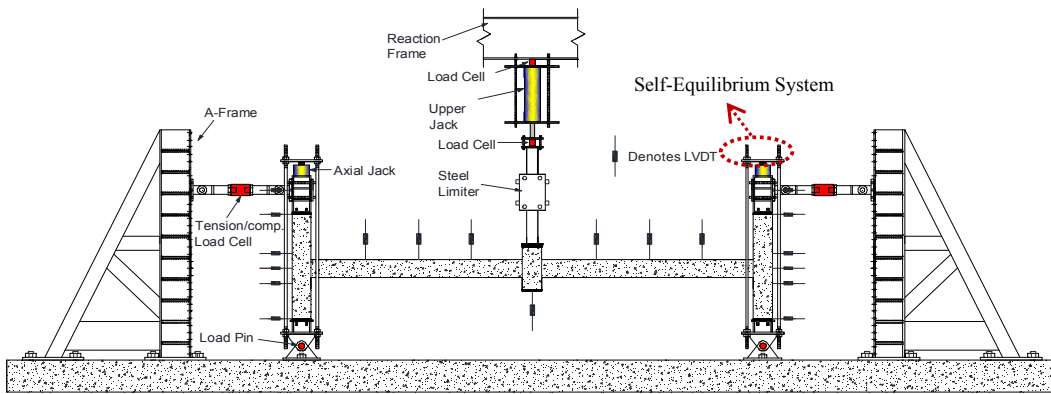
(c) Schematic of simplified boundary condition



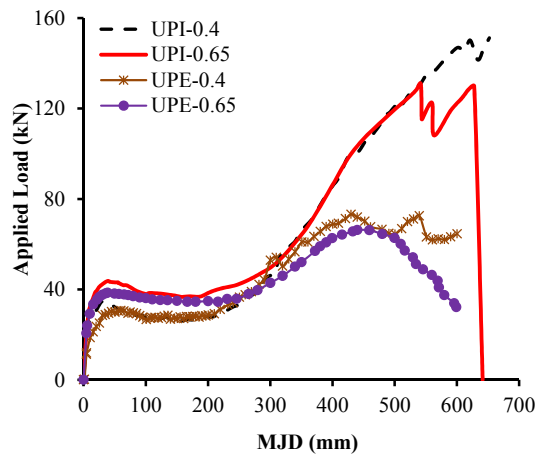
(a)

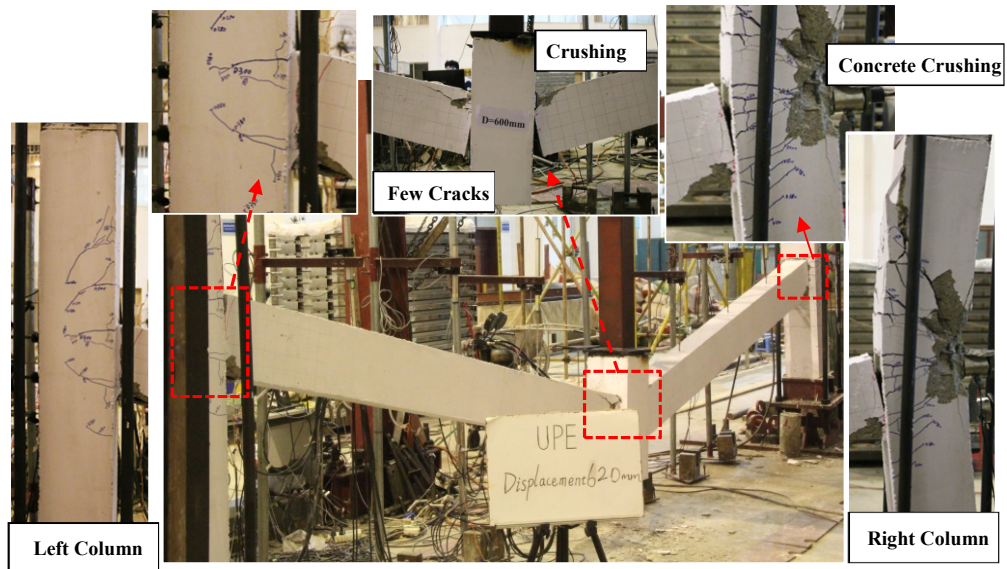


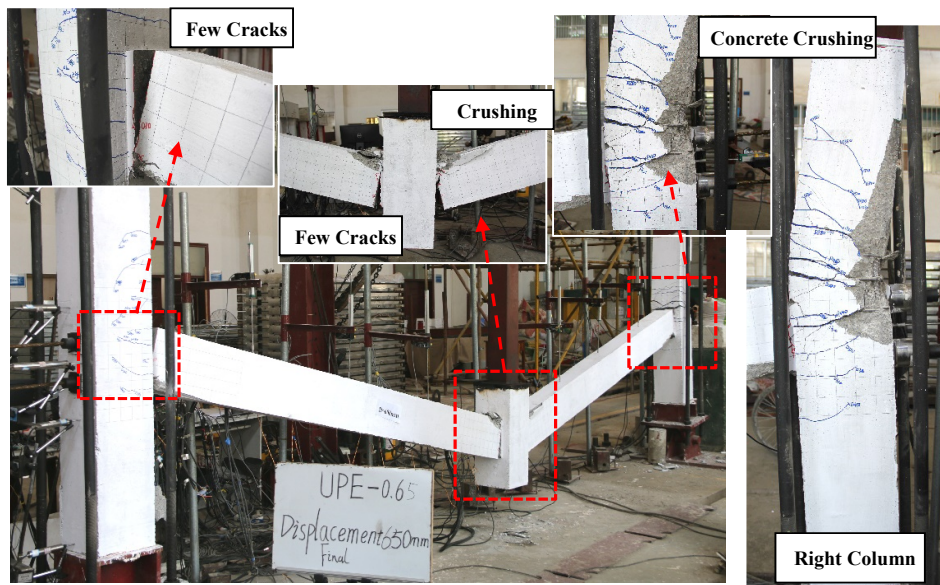
(b)

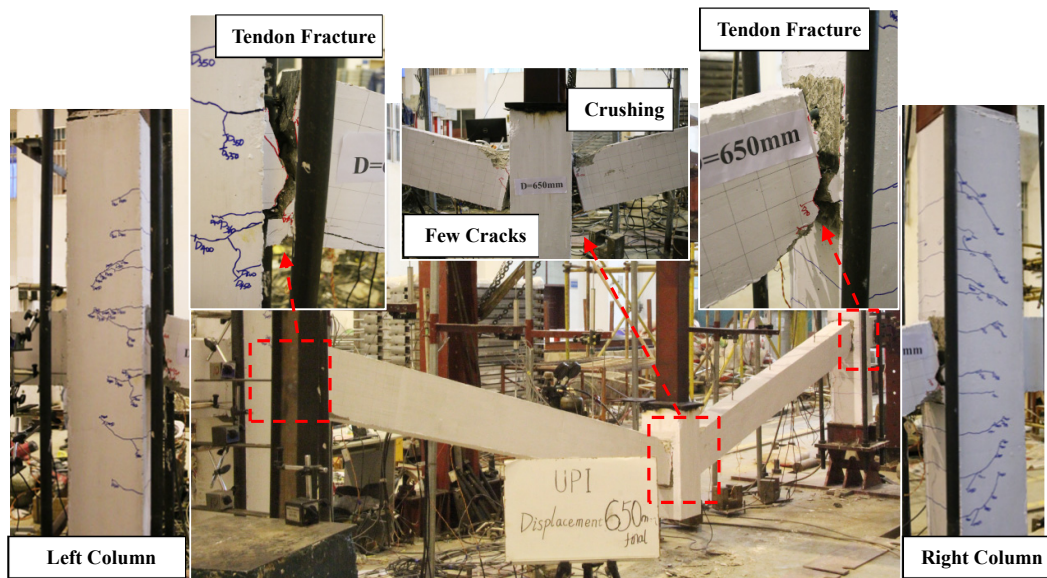


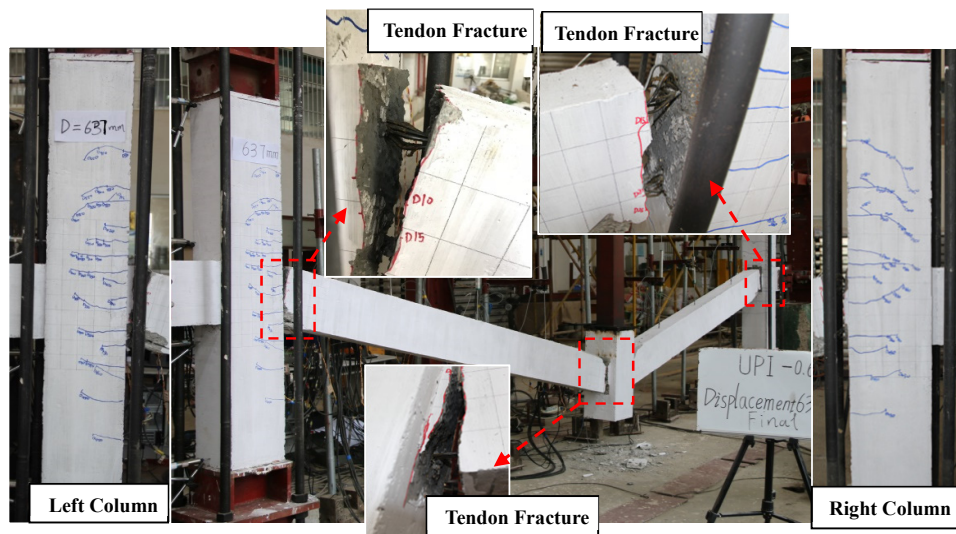
(c)

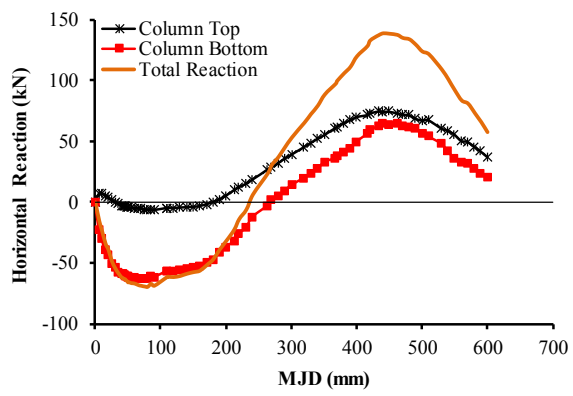




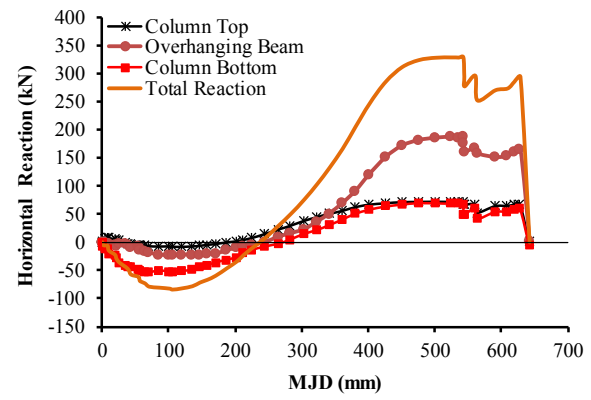




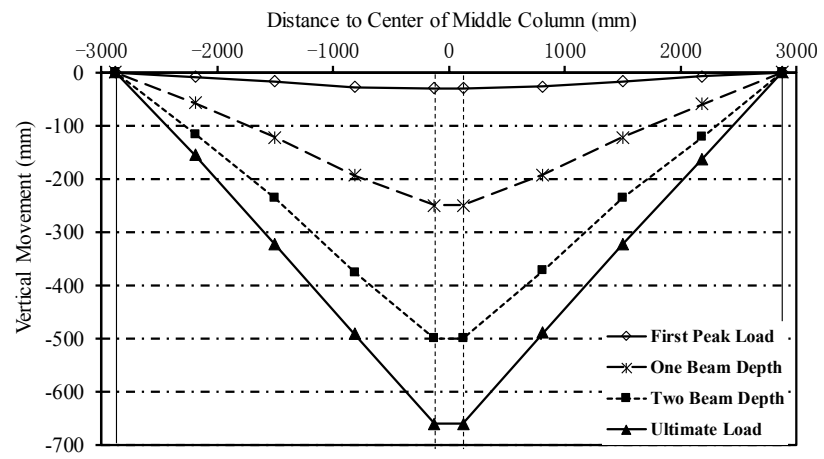


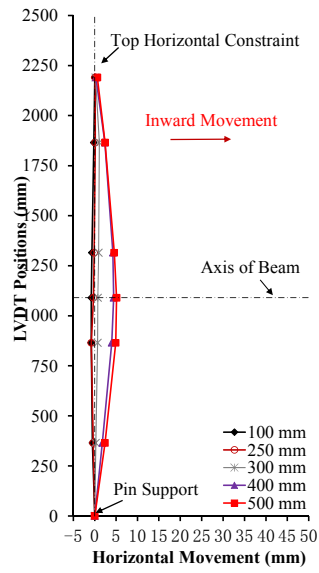


(a)

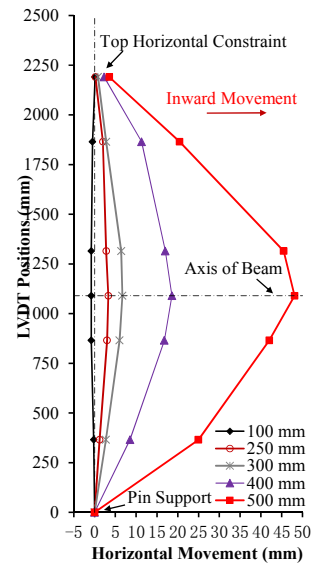


(b)

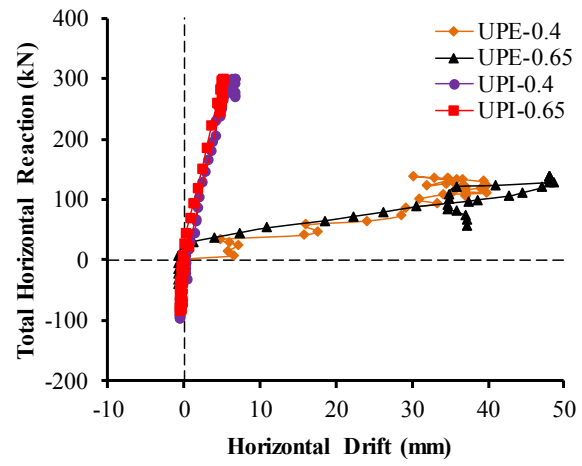


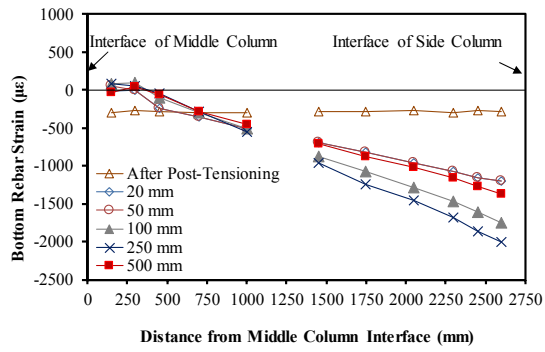


(a)

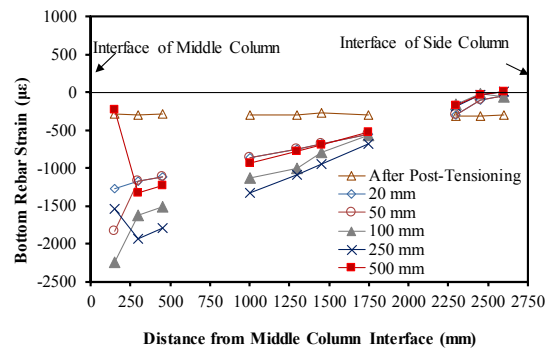


(b)

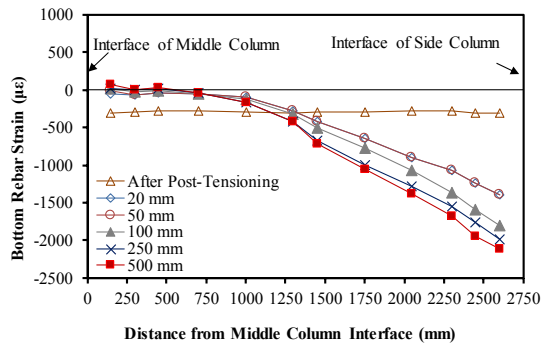




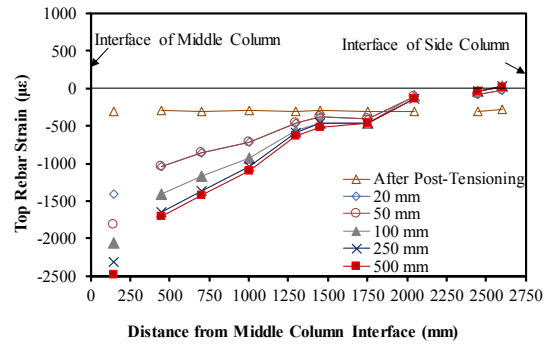
(a)



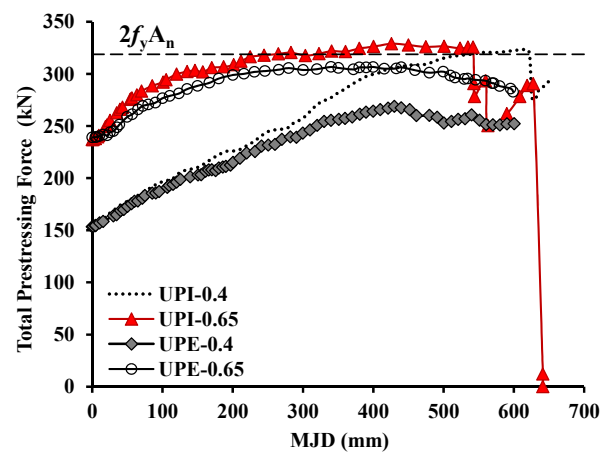
(b)

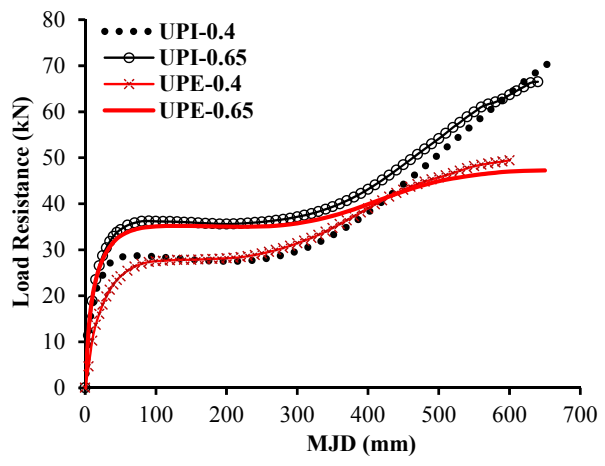


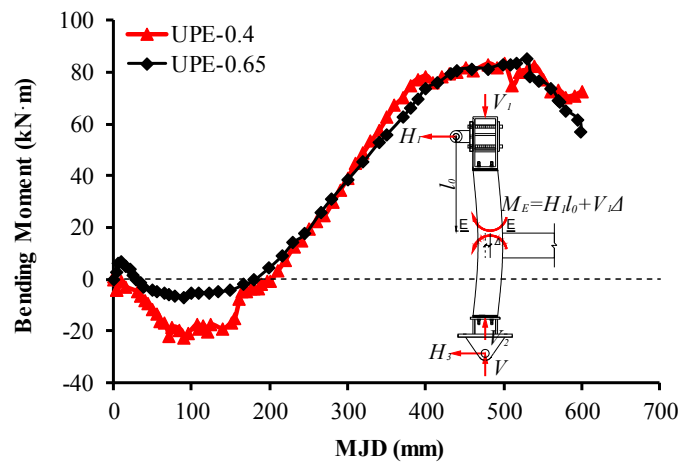
(a)

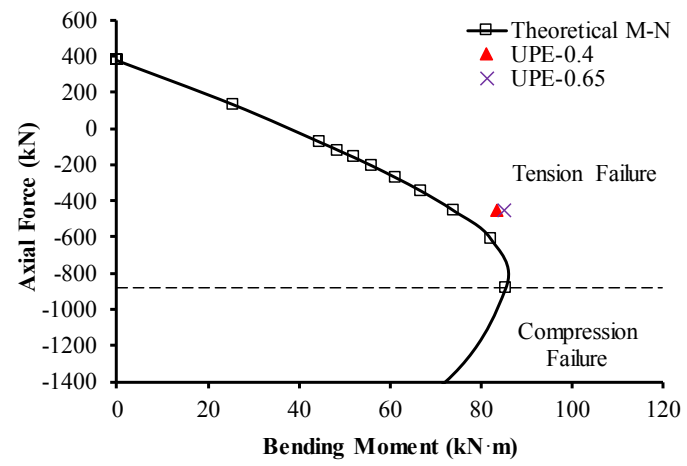


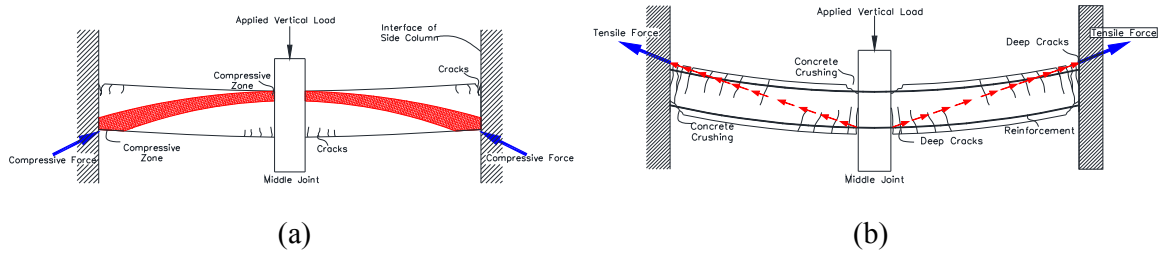
(b)

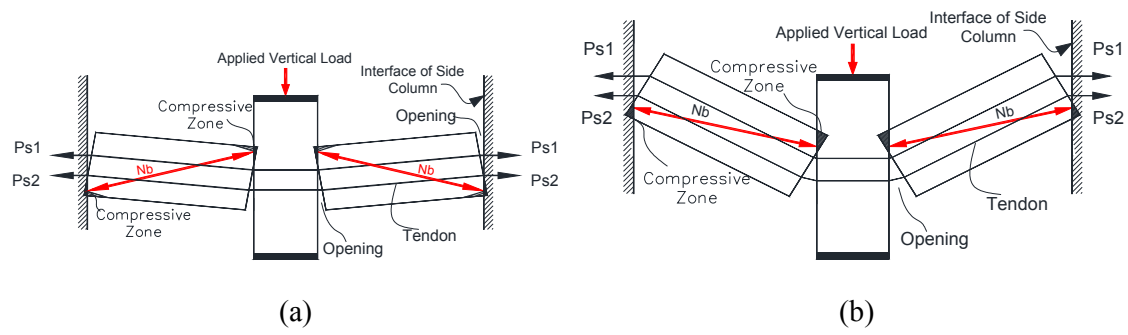


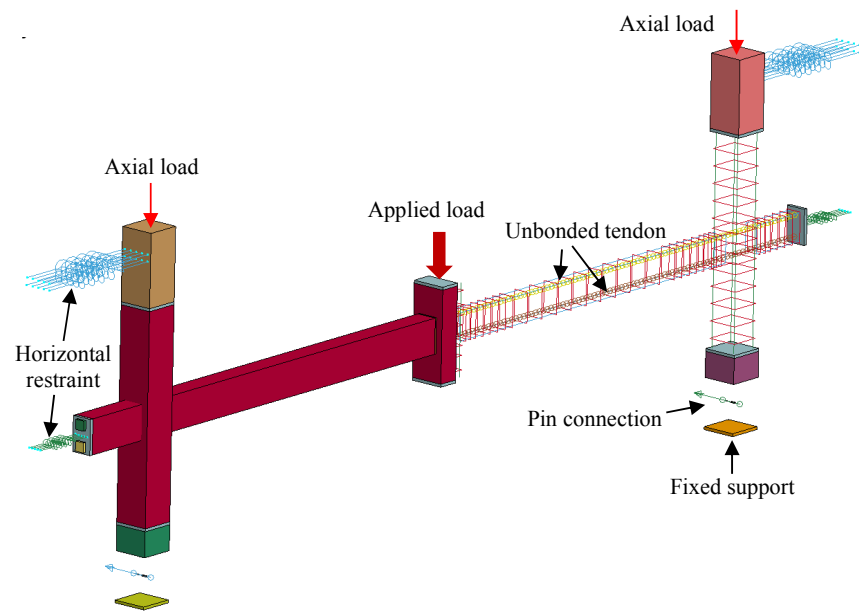


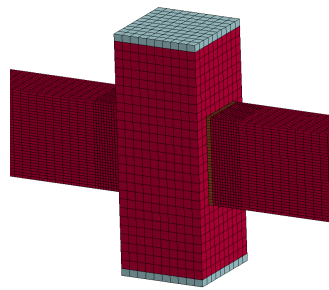




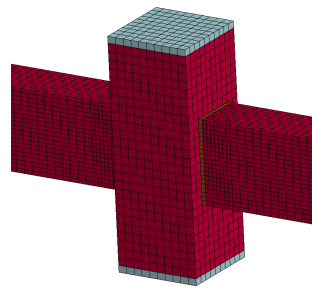




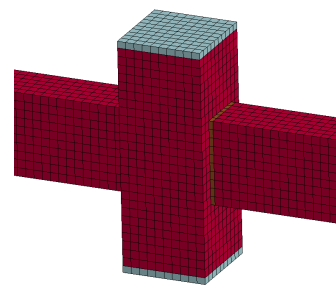




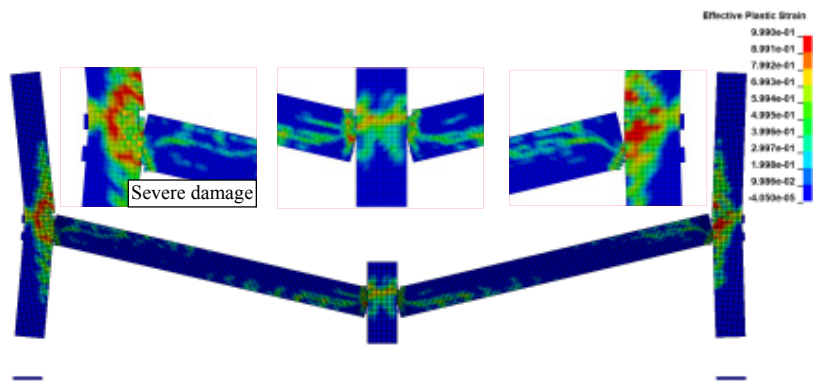
(a)

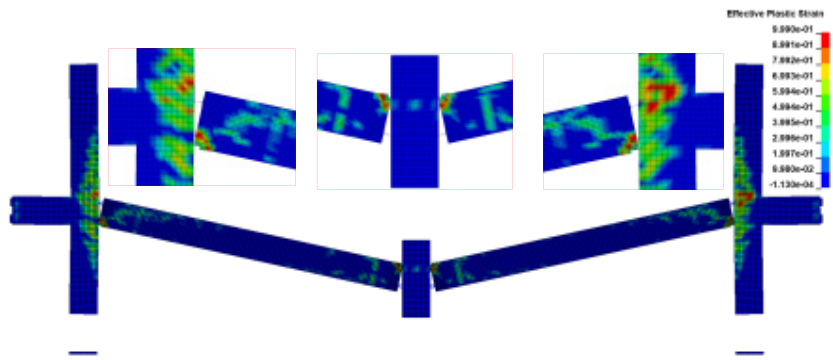


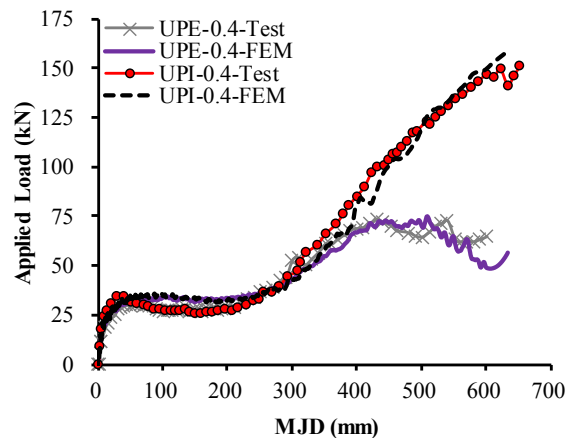
(b)



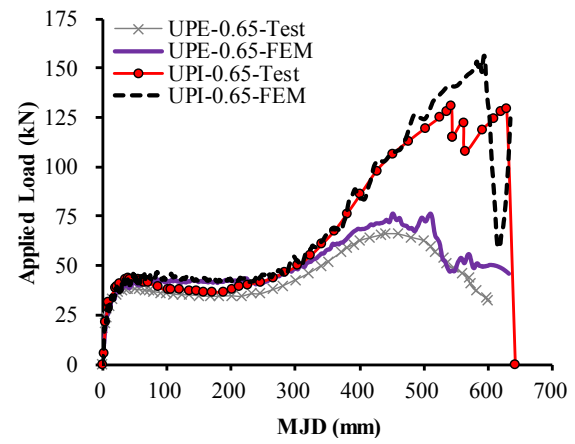
(c)



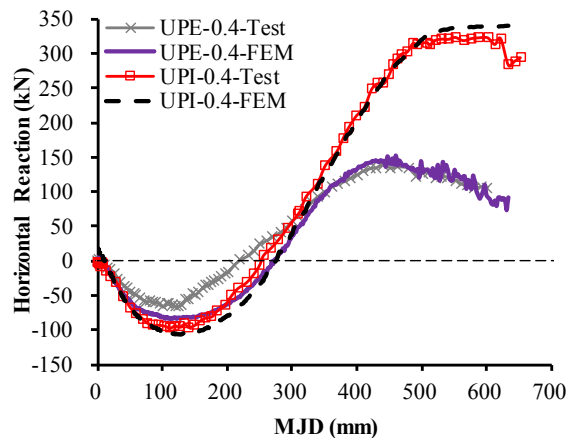




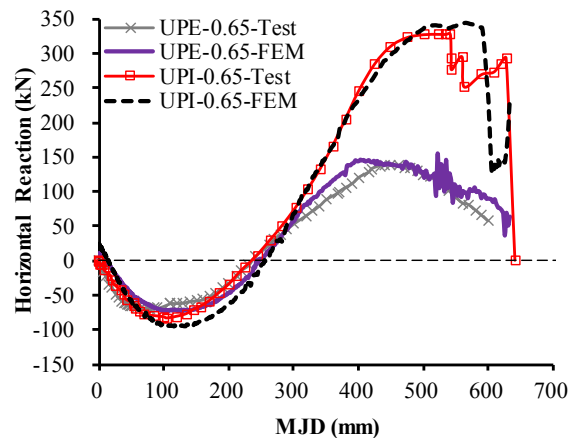
(a)



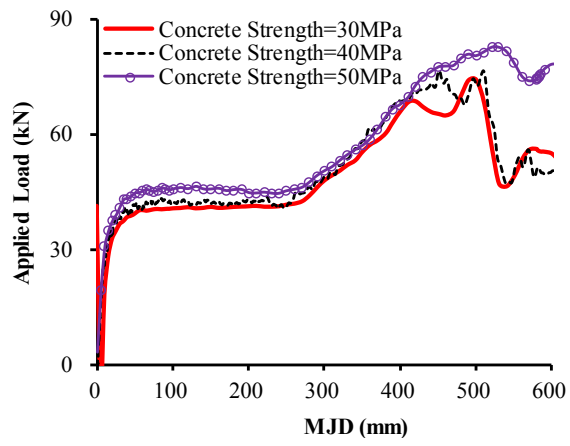
(b)



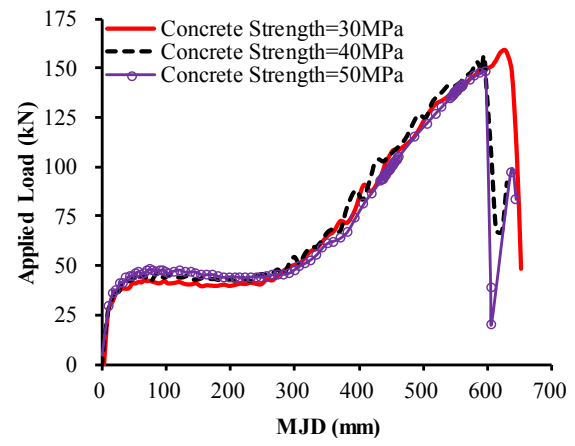
(a)



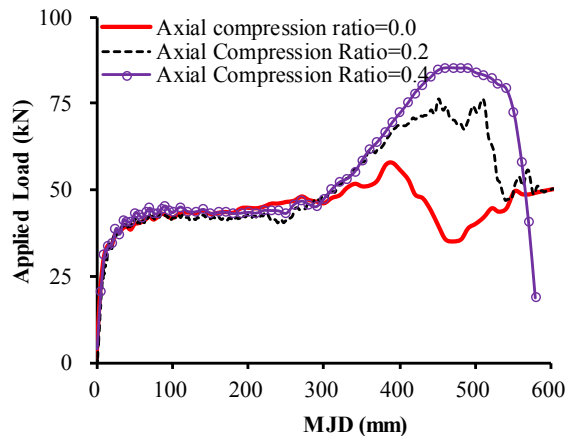
(b)



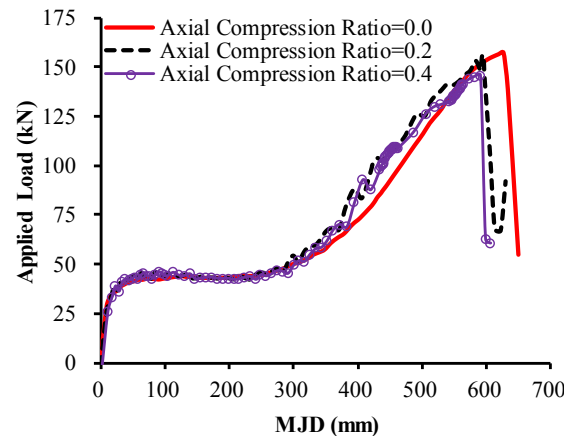
(a)



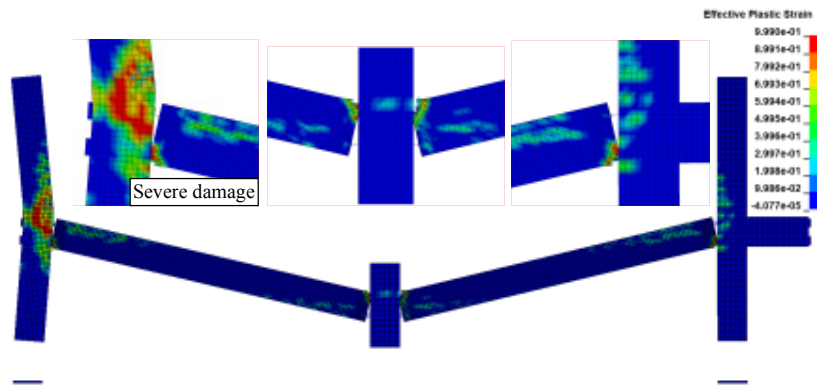
(b)

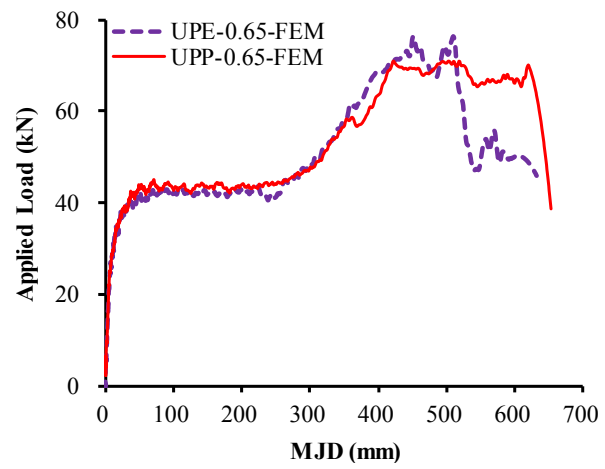


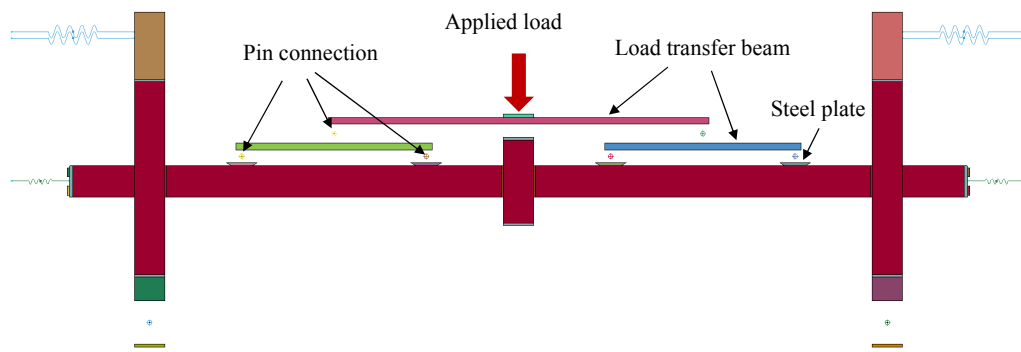
(a)

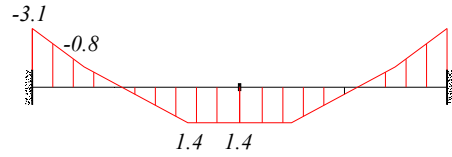
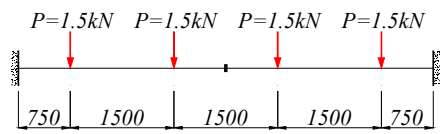
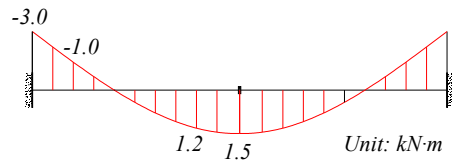
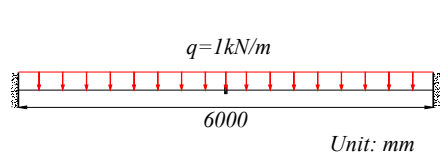


(b)



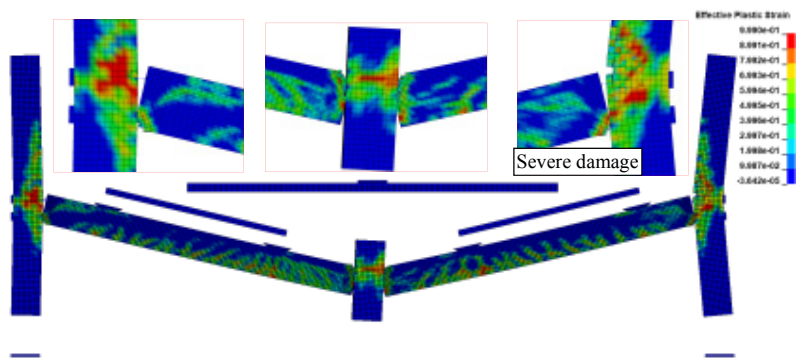


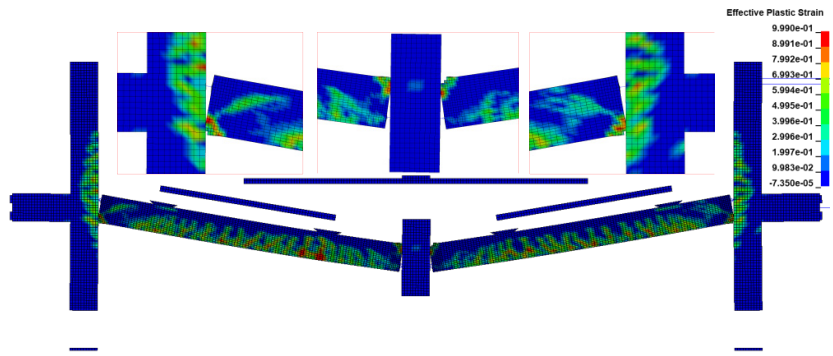


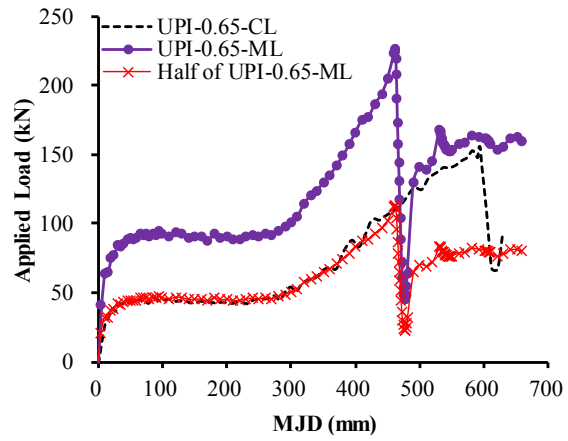


(a)

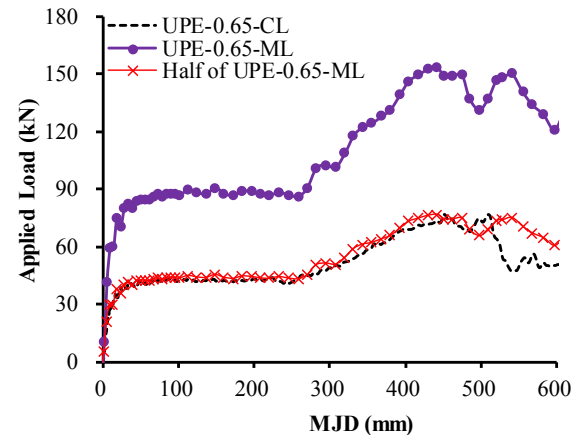
(b)







(a)



(b)